This is a post-peer-review, pre-copyedit version of an article published in Journal of Geodesy. The final authenticated version is available online at: http://dx.doi.org/10.1007/s00190-020-01412-5

New gravimetric-only and hybrid geoid models of Taiwan for height modernisation, cross-island datum connection and airborne LiDAR mapping

Cheinway Hwang[1], Hung-Jui Hsu[1], W.E. Featherstone[2], Ching-Chung Cheng[1], Ming Yang[3], Wenhsuan Huang[1], Chong-You Wang[1], Jiu-Fu Huang[4], Kwo-Hwa Chen[5], Chi-Hsun Huang[1], Hechin Chen[6] and Wen-Yi Su[3]

[1]Dept. of Civil Engineering, National Chiao Tung University, No. 1001, Ta Hsueh Road, Hsinchu, Taiwan.

[2]School of Earth and Planetary Sciences, Curtin University of Technology, GPO Box U1987, Perth, WA 6845, Australia.

[3]Dept. of Geomatics, National Cheng Kung University, No.1, University Road, Tainan, Taiwan.

[4]Dept. of Land Administration, Ministry of the Interior, Taipei, Taiwan.

[5]Dept. of Real Estate and Built Environment, National Taipei University, No. 151, University Road, San Shia, New Taipei City, Taiwan.

[6]National Land Surveying and Mapping Center, Ministry of the Interior, Taichung, Taiwan.

Corresponding author: Cheinway Hwang, cheinway@mail.nctu.edu.tw; cheinway@gmail.com

Abstract

This paper combines gravity data collected from airborne, shipborne and terrestrial surveys and those derived from satellite altimetry to determine a high-resolution gravimetric and hybrid geoid model (on a 30"× 30" grid) in and around Taiwan. Some 6,000 new land gravity values at a 0.03-mGal precision make a notable contribution to the geoid modeling. Shipborne gravity data in waters 20 km offshore Taiwan were collected to improve the coastal geoid precision. In a circular area of 50 km around each of the five major tide gauges in Taiwan, gravity data were measured to improve vertical datum connections between Taiwan and its four offshore islands. Height anomalies were computed first and then converted to geoid heights. At >2000 benchmarks, we obtained measured geoid heights to assess the gravimetric-only geoid and to create a hybrid geoid. Our assessments and formal errors from least-squares collocation indicate few cm of standard deviations for both geoid models, but the gravimetric geoid has mean differences of up to 20 cm with the measured geoidal heights. The hybrid geoid is used in RTK-VBS orthometric heighting, achieving a 5-cm precision. The gravimetric geoid is used to determine the relative differences in the ocean's mean dynamic topography (MDT) between Taiwan and the four offshore islands, which are also compared with those from oceanic and altimetric methods for estimating MDT. Differences in MDT help to identify 41.7 cm and 54.1 cm offsets in the current vertical datums of Penghu and Lanyu islands. In a low-lying, flood-prone region of southern Taiwan, the hybrid geoid improves LiDAR mapping of sub-zero elevation zones by 20 cm, corresponding to 70 years of sea level rise at an assumed rate of 0.286 cm/yr.

Keywords: geoid; height modernization; LiDAR; oceanic mean dynamic topography; Taiwan; vertical datum unification

1. Introduction

A geoid model comprises a basic national mapping infrastructure for modern geodetic surveying and has benefited economic developments by providing low-cost, physical (orthometric) heights needed in most engineering works. Many nations have invested considerable resources in constructing high-precision and high-resolution gravimetric geoid or quasi-geoid models. For example, since the 1990s, the National Geodetic Survey (NGS) of the USA have released several gravimetric and hybrid geoid models (https://www.ngs.noaa.gov/GEOID/). The latest US geoid model is Geoid2012, and NGS's geoid modeling is improving with the input of new gravity data from the Gravity for the Re-definition of the American Vertical Datum (GRAV-D) project carried out over 2008–2022 (e.g., Johnson, 2009). Mainland China has constructed a number of quasi-geoid models, which were reported by many Chinese scholars and agencies such as Chinese Academy of Surveying and Mapping (http://english.casm.ac.cn/). A new Canadian geoid model was released and documented by Huang and Véronneau (2013). In Japan, the latest geoid modeling effort was reported by Miyahara et al. (2014). The latest Australian quasi-geoid model was released in 2018, featuring error estimates (Featherstone et al., 2018). In addition, there have been many past and ongoing projects to construct geoid models in the European Union (Denker et al., 2009), Africa, Southeast Asia, and South America (see http://www.isgeoid.polimi.it).

A quality geoid model depends on many factors; although one could optimize the numerical method of geoid modeling, gravity data remain a dominant factor in the resulting geoid precision. Therefore, much of the effort has been placed on gravity data collections, e.g., in such a project like GRAV-D initiated by the National Oceanic and Atmospheric Administration (NOAA; https://www.ngs.noaa.gov/GRAV-D). The airborne gravity from GRAV-D has been shown to improve geoid precision over the

Great Lakes region (Li et al., 2016) and more improved US geoid models are expected from GRAV-D. However, gravity data alone cannot result in a geoid model that can be directly used in orthometric heighting using Global Navigation Satellite System (GNSS) and Light Detection and Ranging (LiDAR) measurements, because the underlying vertical datum of a gravimetric model can deviate from a local vertical datum that is typically realized by a network of control points where the orthometric heights are obtained by precision leveling relative to the zero of the local vertical datum. On the other hand, observed geoidal heights at these control points can be blended with the gravimetric geoid model to produce a hybrid geoid model that can be directly used for orthometric heights. Sample hybrid geoid models for direct orthometric heighting are the GEOID12B model for the USA, and national models by Featherstone et al. (2018) for Australia, Huang and Véronneau (2013) for Canada, Li (2012) for mainland China, and Denker et al. (2009) for Europe.

Developing a high-resolution geoid model in a region like Taiwan requires a considerable effort in gravity data collection and numerical techniques. Taiwan is surrounded by the Pacific Ocean to the east with deep trenches, the South China Sea to the south, the Taiwan Strait to the west and the East China Sea to the north. The terrain of Taiwan is mostly rugged (up to 4000 m high), with flat regions only on its coastal plains. Land-based gravity surveys can only be conducted along mountain treks and areas suitable for walks or vehicle transportation. Despite these difficulties in geoid modeling, a precision geoid in Taiwan is needed because of the following issues. First, three-dimensional, real-time cm-level positioning has been realized by the use of a continuous GNSS network (see Section 5.1). Real-time precise orthometric heighting by GNSS is not possible without a geoid model that fits the real-time positioning. Second, the Kuroshio Current east of Taiwan and the surrounding seas create large gradients in the dynamic ocean topography around Taiwan that can cause large differences in the vertical datums between Taiwan and its offshore islands. The differences cannot be resolved without a precise geoid model. Finally, the ellipsoidal heights of the entire Taiwan and most parts of Taiwan's offshore islands have been measured by LiDAR. Converting such ellipsoidal heights to orthometric heights requires a precise geoid model. In low lying areas and foothills, the accuracy of a geoid model can be critical to assessing flooded zones and geohazards (landslides) due to highly sloping terrains.

Despite Taiwan's difficult terrain, the current gravity data coverage in Taiwan is relatively dense and uniform, thanks to several land-, sea- and air-borne gravity surveys (Hwang et al., 2014). In addition, a vertical datum connection project of Taiwan over 2008–2011 was carried out to collect ship-borne gravity data within a 50-km circular area around each of the five tide gauges in Taiwan and its offshore islands, where the tidal records defined the current mean sea levels that in turn define their vertical datums. These dedicated gravity surveys produced gravity anomalies around the tide gauges for high-precision geoidal heights, which can be used to validate the vertical datums of the offshore islands and unite with the vertical datum of Taiwan. The objectives of this paper are (1) to show the development of the new Taiwan geoid models and (2) to show how the models can benefit real-time orthometric heighting, cross-island vertical datum connection and LiDAR mapping.

2. Data for geoid modeling and assessment

2.1 Land and airborne gravity measurements

The terrestrial (land and near shore) gravity data used in this paper are classified into three categories as follows (Fig. 1a-c).

(1) Land gravity data (Fig. 1a)

We classify this dataset into two sub-sets. Sub-set 1 contains point gravity measurements collected over 1980–2003 at Taiwan's horizontal control points and first-order benchmarks. The point gravity data on the first-order benchmarks were collected in the 1990s and 2000s. Sub-set 2 contains point gravity measurements collected over 2004–2006. Except gravity measurements made on the horizontal control points, all gravity values are assigned with standard errors using the results of network adjustments (Hwang et al., 2003). The standard errors range from tens of μgal to nearly one mgal. The gravimeters used for data collection were LaCoste and Romberg (LCR) Model G, Graviton-EG and Scintrex CG-5 gravimeters.

(2) Airborne gravity data (Fig. 1b)

Over 2004–2009, three airborne gravity surveys were carried out to collect gravity data over Taiwan at a mean altitude of 5156 m (Hwang et al., 2007; Campaign 1) and an area over the Kuroshio Current east of Taiwan, and an area over the eastern half of the Taiwan Strait, both at an altitude of 1620 m (Hwang et al., 2012; Campaigns 2 and 3). The distributions of gravity data collected in these three campaigns are shown in Fig. 1b. Details about the gravity data collection and processing have been presented in Hwang et al. (2014) and will not be repeated here.

2.2 Offshore shipborne gravity measurements (Fig. 1c).

The offshore gravity data in Fig. 1c were collected within 50 km to the five tide gauges (Fig. 1d) and over waters 20 km offshore Taiwan. The aim of these new coastal gravity measurements was to improve the geoid height accuracy at offshore islands of Taiwan for an improved vertical datum connection between Taiwan and these islands, and for an improved coastal geoid model. The decision to collect such coastal gravity data was also driven by the increasing need of LiDAR mapping of coastal plains in Taiwan. Although satellite altimetry can yield offshore gravity anomalies, their precision is much lower than in the open oceans. The airborne gravity data (Fig. 1b) may contribute gravity signals to the offshore and immediate coastal areas (Fig. 1b), but they are less accurate than the land-based gravity values and they contribute to geoidal signals only at several km wavelengths, due to altitude attenuation of gravity.

Table 1 shows information about the shipborne gravity surveys from 2006 to 2010 near the five tide gauges where the mean sea levels are the origins of the vertical datums for Taiwan (the main island), Penghu (PH), Liuqiu (LQ), Ludao (LD) and Lanyu (LY) (Fig. 1c). As stated earlier, the surveyed areas are within 50 km to the five tide gauges. For the north-south lines, the line spacing is 2´ for lines within 0-20 km to the tide gauges, and the spacing is 4´ for lines within 20 to 50 km. The line spacings for the west-east lines are kept at about 17 km, while for the west-east lines, the spacing is 8.5 km for lines 20 km to the tide gauges, and 17 km beyond 20 km. The gravimeters used are L&R Air-Sea Ⅱ (LCR, 2003) and ZLS Dynamic Gravity Meter, with a sampling rate of 1 Hz. The tonnage of the ships carrying the gravimeters is about 16. To avoid large noise, we carried out surveys only under the condition that oceanic wave heights were below 1 m. The ship positions were determined by post-processing dual-frequency carrier phase kinematic GPS using the Bernese software version5.2 (Dach et al., 2015). The raw gravity measurements were corrected for the effects of solid Earth and ocean tides. The resulting 1-Hz gravity anomalies were then filtered using a Gaussian filter with window widths ranging from 120 s to 150 s. The filtering results in a spatial resolution of about 500 m. The crossover analysis indicates that the precisions of such shipborne gravity anomalies are about 0.65–1.94 mGal.

Table 2 shows information about the offshore shipborne gravity surveys that were carried out in 2011-2013. The gravimeters and the ships are similar to the ones shown in Table 1. The survey lines cover the 20-km shallow waters around the entire Taiwan. Over some areas of these surveys, the lines are sparse because these areas are overlapped with areas around tide gauges (Table 1). The same filter and corrections as those used for the result in Table 1 were applied to the raw gravity values. The gravity anomaly precisions range from 1.32 mGal to 2.36 mGal.

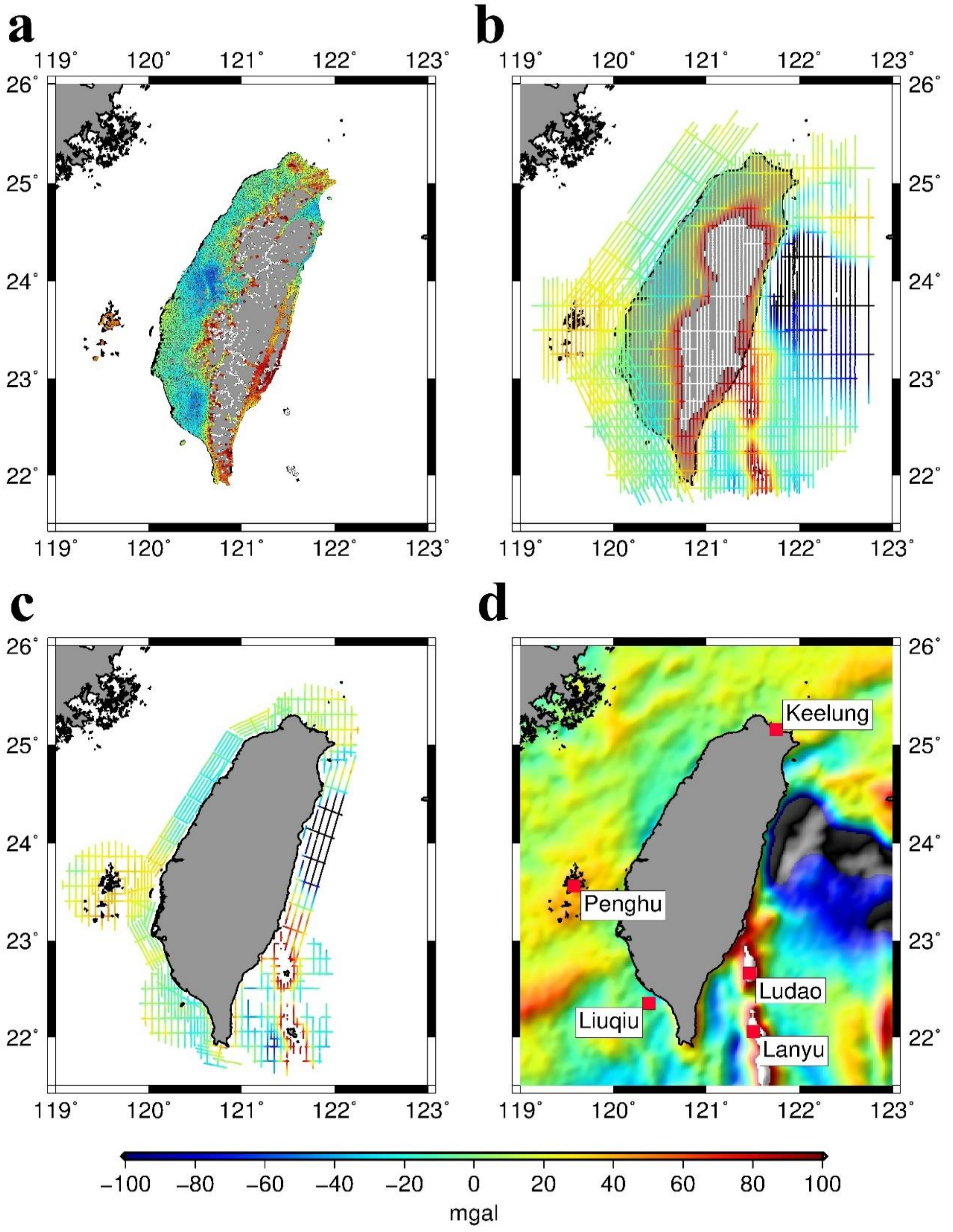

Fig. 1: Free-air gravity anomalies around Taiwan from (a) land (point) measurements, (b) airborne surveys, (c) coastal ship surveys, and (d) satellite altimetry. The gravity data in Fig. 1c is mainly for improving the geoidal heights at the key tide gauge stations of main island of Taiwan (KL) and the four offshore islands Penghu (PH), Ludao (LD), Lanyu (LY) and Liuqiu (LQ).

Table 1: Information about the shipborne gravity surveys within 50 km to five tide gauges

Tide gauge	Keelung	Liuqiu	Ludao	Lanyu	Penghu
Year	2006	2006	2007–2008	2008–2009	2010
Gravimeter	L＆R S130	L＆R S130	L＆R S130	ZLS Dynamic Gravimeter	ZLS Dynamic Gravimeter
No. of points[a]	1760	1923	1737	1939	1906
Filter width (second)	120–150	120–150	120–150	120–150	120–150
Crossover diff. (mGal)	1.63	1.94	0.65	1.59	0.88
No. of crossovers	35	41	42	59	60

[a]Filtered gravity values at 0.5 km intervals

Table 2: Information about the coastal gravity surveys in three offshore areas (20 km to shores) around Taiwan

Area	Southwest coast	Northwest coast	East coast
Year	2011	2012	2013
Gravimeter	ZLS Dynamic Gravimeter	ZLS Dynamic Gravimeter	ZLS Dynamic Gravimeter
No. of points[a]	2329	2947	2259
Filter width (second)	120–150	120–150	120–150
Crossover diff. (mGal)	1.32	2.36	2.09
No. of crossovers	41	34	21

[a]Filtered gravity values at 0.5 km intervals

2.3 Marine gravity from satellite altimetry (Fig. 1d)

In order to fill in the data gaps in the shipborne gravity at sea and along the coasts of Taiwan, we used altimeter-derived sea surface heights (SSHs) to determine marine gravity anomalies around Taiwan. We used SSHs altimeter data from both the repeat and non-repeat missions. The repeat missions include Geosat/ERM, ERS-1/35d, ERS-2/35d, ENVISAT and the T/P–series satellites (TOPEX/Poseidon, Jason-1 and Jason-

2). The SSHs from the repeat missions were averaged (stacked) to reduce errors caused by noise and systematic errors in environmental corrections such tide model errors and atmospheric delays. The non-repeat altimeter data are from the missions Geosat / GM, retracked ERS-1/GM, Jason-1/GM and CRYOSAT-2. Except for CRYOSAT-2, all waveforms were retracked by the sub-waveform threshold retracker (Yang et al., 2012) to correct for the errors caused by corrupted waveforms in the shallow waters around Taiwan. Table 3 shows the altimeter data sets used in this paper.

Around the coastal waters of Taiwan, SSHs from these altimeter missions are prone to systematic errors (especially tide model errors and waveform-induced errors). It is possible, but difficult, to remove such errors by a crossover adjustment of SSHs. As such, we used SSH-derived geoid gradients and the method of the inverse Vening Meinesz (IVM) (Hwang, 1998) to compute marine gravity anomalies around Taiwan. In the IVM method, along-track geoid gradients were derived from along-track SSHs, followed by gridding the gradients on a north-south grid and on an east-west grid, and finally by one-dimensional (1-D) FFT computations to determine gravity anomalies on the same grid (Hwang et al., 2006). Fig. 1d shows the marine gravity anomalies around Taiwan derived from the altimeter data listed in Table 3. The precision of the altimeter-derived gravity anomalies is at the 8-mGal level (Hwang et al. 2014), depending on the gravity roughness, water depth, and the data density and quality of the altimeter measurements.

A band-limited least-squares collocation method (Hwang et al., 2014; Shih et al., 2015) was used to form a 0.5′×0.5′grid of free-air gravity anomalies from the gravity data described in Section 2.1 and 2.2 and the altimeter-derived marine gravity in Section 2.3. The resulting free-air gravity anomalies and planar complete/refined Bouguer gravity anomalies are shown in Fig. 2. The planar terrain corrections for the Bouguer gravity anomalies were computed using the Gaussian quadrature method (see Section

3.1 and Hwang et al., 2003) and the latest Taiwan digital elevation models (see Section 2.4). For each grid point of the gridded free-air gravity anomalies (Fig. 2a), we selected gravity data (Table 1) within a 0.5° window around the grid point and carried out the band-limited least-squares collocation computation using the covariance functions belonging to the different gravity datasets in Table 1 (Shih et al., 2015). This point-wise computation avoided inversions of large matrices.

Table 3: Altimeter data for deriving marine gravity anomalies around Taiwan

Satellite	Repeat period (day)	Height (km)	Inclination (°)	Spacing at equator (km)
Geosat/GM	No	788	108	4
ERS-1/GM	No	781	98.5	8
Jason-1/GM	406	1324	66	7.7
Geosat/ERM	17	788	108	165
ERS-1/35d	35	781	98.5	80
ERS-2/35d	35	785	98.5	80
T/P–series[a]	10	1336	66	280
Cryosat-2	369	717	92	7.5

[a]TOPEX/Poseidon, Jason-1, and Jason-2

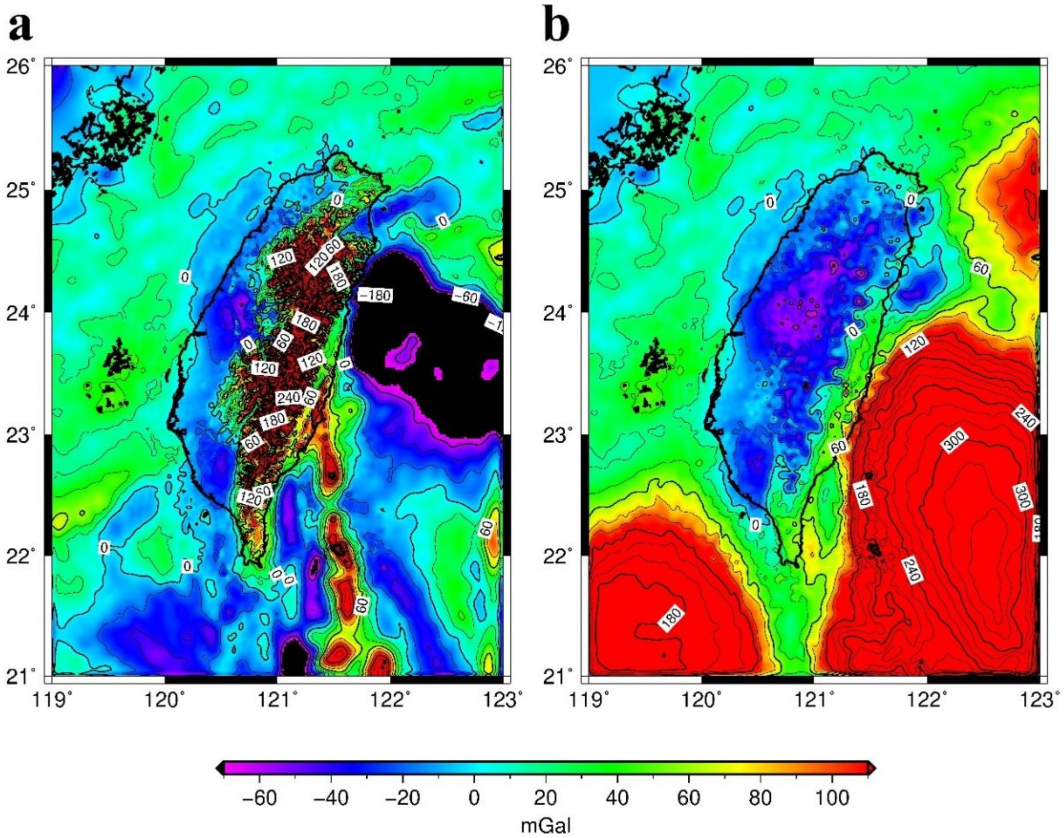

Fig. 2: The (a) free-air gravity anomalies and (b) refined/complete planar Bouguer gravity anomalies around Taiwan from all gravity data sources (Fig. 1a-d).

2.4 Digital elevation model and observed geoid heights

2.4.1 Digital elevation model (DEM)

DEMs are used for computing terrain corrections when generating Faye gravity anomalies (see Section 3.1). The DEMs are from several years of photogrammetric surveys and are originally available on a 40×40 m grid (Hsiao and Hwang, 2010). We used this grid to generate a DEM on a 3"×3" grid, which was then filtered to create a 9"×9" DEM. The 3"×3" and 9"×9" DEMs were used to compute the inner and outer zone contributions of the planar terrain corrections using Gaussian quadrature (Hwang et al., 2003).

2.4.2 GPS-observed geoidal heights at leveling benchmarks

A GPS-observed geoidal height at a leveling benchmark is the difference between the ellipsoidal height and the orthometric height. The purpose of the observed geoidal heights is twofold: (1) assessing the gravimetric geoid model (only selected benchmarks are used for this assessment, see Section 3.1), and (2) merging with the gravimetric geoid model to create the hybrid geoid model (Section 3.2). The ellipsoidal heights were determined by GPS using various session lengths. The orthometric heights were determined by precision leveling that requires double-run misclosures of 2.5-3 mm$\sqrt{k}$, where k is the distance (in km) between two neighboring benchmarks. The orthometric heights are defined in the Taiwan Vertical Datum (TWVD2001) height system (Yang et al., 2003), for which the zero elevation is at the mean sea level at Keelung Harbour in northern Taiwan (Keelung in Fig. 1c).

Three groups of observed geoid heights are used and their point distributions are shown in Figs. 3a-c. The GPS session lengths range from one hour to 24 hours, with formal height errors at the levels of sub-cm to few cm as provided by Bernese V5.2. The times of the GPS observations (for ellipsoidal heights) and precision leveling (for orthometric heights) are different and the observed geoidal heights are affected by vertical deformations due to land subsidence and uplift. To compensate for the effect of vertical land motion, for each point in Fig. 3a-c, we reduced the original GPS-derived ellipsoidal height to a height corresponding to the measurement time of the orthometric height, based on the vertical velocity model of Chen et al. (2011).

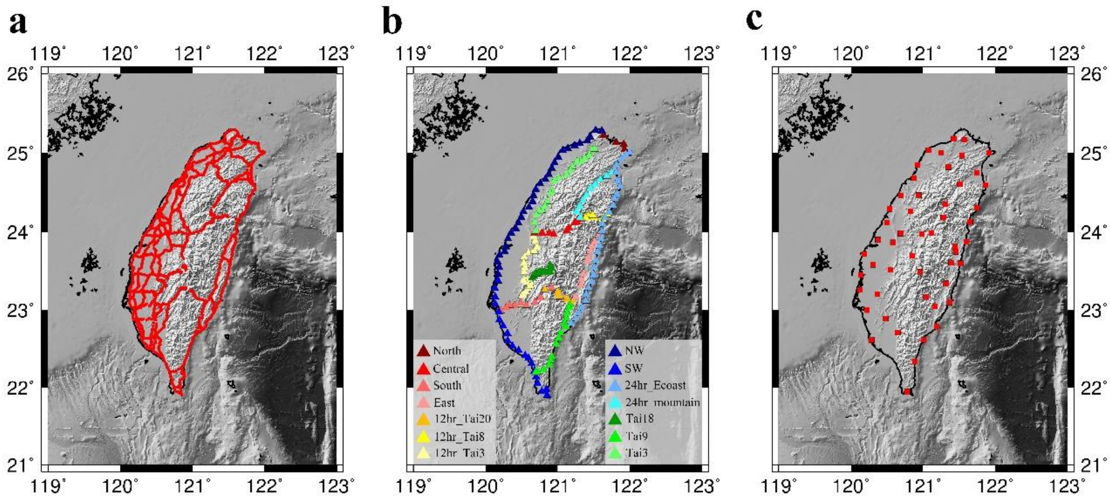

Fig. 3: Distribution of benchmarks with GPS-observed geoidal heights for assessing the gravimetric geoid and for creating the hybrid geoid model. (a) first-order leveling benchmarks (1920 points; 1–3 hour GPS session length), (b) coastal and interior benchmarks (214 points; 12–24 hour GPS session length), (c) 52 eGNSS Stations (eGNSS is a continuous station for real-time positioning; see Section 5.1). All such geoid heights are used for creating the hybrid geoid, but only those in Fig. 3b, c are used for geoid precision assessments (excluding four anomalous benchmarks in Fig. 3b). The symbols in Fig. 3b are associated with the leveling routes in Tables 4 and 5.

3. Numerical method for geoid computation

3.1 The gravimetric geoid model

There are several methods for geoid and quasigeoid modelling in the geodetic literature. The method we choose is presented below. This paper adopts the "modern" approach that is based on gravity anomalies on the ground and the use of planar terrain corrections (Section 48, Moritz, 1980). That is, height anomalies are determined first, followed by conversion to geoidal heights. Fig. 4 shows the flowchart for the determinations of the gravimetric and hybrid geoid models. This method requires

Taiwan's regional gravity values, a global geopotential model and a DEM. The first product is the gravimetric geoid, which is used to construct the hybrid geoid model using the observed geoid heights (Section 2.4). The method is divided into four steps (Fig. 4). In Step 1, all gravity data (Section 2) are merged to create grids of free-air and Bouguer anomalies (Fig. 2a and b). In Step 2, residual gravity anomalies $d\Delta g_F$ are obtained by subtracting the reference value Δg_{ref} from the full gravity anomaly Δg as:

$$d\Delta g_F = \Delta g - \Delta g_{ref} \tag{1}$$

We experimented with different maximum harmonic degrees for EGM2008 (Pavlis et al., 2012, 2013) to generate a "best" Δg_{ref} in Eq. 3, and found that degree = 2190 yields the best geoid model precision. Because of the use a degree-2190 reference field, we do not use the residual terrain model in our geoid modeling (Forsberg, 1984). The use of EGM2008 is justified by the fact that earlier land gravity (Hwang, 1997) have been used by the EGM2008 Development Team. In Step 3, the terrain correction (TC) and Faye gravity anomaly $d\Delta g_{Faye}$ are computed as (Moritz, 1980, p. 415)

$$C = \frac{G\rho R^2}{2} \iint_\sigma \frac{\left(H' - H\right)^2}{l_0^3} d\sigma \tag{2}$$

$$d\Delta g_{Faye} = d\Delta g_F + C \tag{3}$$

where

C: terrain correction

G: gravitational constant

ρ: rock bulk density (2.7 g/cm^3) for Taiwan

R: Earth's mean radius; 6371 km is used

H': elevation from the DEM (Section 2.4)

H : elevation at the gravity data point

l_0 : Horizontal distance between the points with H' and H

$d\sigma$: differential spherical surface area

In Eq. 3, gravity anomalies on the topographic surface are needed and practically equal to gravity anomalies on the geoid at sea level (see Fig. 2a; for the theory see Heiskanen and Moritz, 1967, p. 310). In this paper, the planar TC in Eq. 2 was computed by the method of Gaussian quadrature (Hwang et al., 2003), with the 3"×3" DEM for the inner zone and the 9"×9" DEM for the outer zone (Section 2.4.1). The Faye gravity anomalies were used to compute residual height anomalies ζ_{res} using the following integral (Heiskanen and Moritz, 1967) and 1-D FFT implementation (Haagmans et al., 1993):

$$\begin{aligned} \zeta_{res} &= \frac{R}{4\pi\gamma}\iint_{\sigma} d\Delta g_{Faye} S_M(\psi) d\sigma \\ &\approx \frac{R\Delta\phi\Delta\lambda}{4\pi\gamma}\sum\cos\phi\sum d\Delta g_{Faye}\cdot S_M(\psi) \\ &= \frac{R\Delta\phi\Delta\lambda}{4\pi\gamma} F_1^{-1}\left[\sum F_1\left\{S_M(\psi)\right\} F_1\left\{d\Delta g_{Faye}\cos\phi\right\}\right] \end{aligned} \quad (4)$$

where γ is normal gravity, $\Delta\phi$ and $\Delta\lambda$ are grid intervals along latitude and longitude, respectively, F_1 and F_1^{-1} are the forward and inverse 1-D FFT operators for a latitudinal belt. The Wong and Gore (1969) modified Stokes kernel S_M in Eq. 4 is

$$S_M(\cos\psi) = \sum_{n=M+1}^{\infty}\frac{2n+1}{n-1}P_n(\cos\psi) \quad (5)$$

where M is the degree of truncation and P_n is the Legendre polynomial of degree n. Eq. 5 is used to compensate for the errors in the gravity anomalies and the removal of the reference gravity. We experimented with several M values and found that M=108 yields the best geoid precision. That is, using M=108 results in the smallest root-mean-square difference between the gravimetric geoid heights and the GPS-levelling-observed geoid heights at the benchmarks in Fig. 3b.

The use of the terrain-corrected (Faye) gravity anomalies implies that the telluroid has been changed (Heiskanen and Moritz, 1967, p. 322). We compensate for this change using the first-order indirect effect (Moritz, 1980, Eq. 48-29; Sjöberg, 2000, Eq. 7a, 78b).

$$\delta\zeta_{Ind} = \frac{\pi G \rho H^2}{\gamma} \tag{6}$$

where H is the orthometric height. Figure 5 shows the indirect effects around Taiwan. The effects can be up to 50 cm in high mountains (elevations >3000m). Our numerical experiments show that, without the indirect effects in the gravimetric modeling, the errors of the modeled geoidal heights are significantly amplified. In addition, higher-order indirect effects were given by Sjöberg (2000, Eq. 20) and require numerical integrations over the entire sphere. Such effects were not investigated in this paper.

By restoring the long wavelength contribution to height anomaly (ζ_{ref}) associated with the reference gravity anomaly Δg_{ref}, and by adding the indirect effect from Eq. 6, we obtain the height anomaly

$$\zeta = \zeta_{ref} + \zeta_{res} + \delta\zeta_{Ind} \tag{7}$$

which is converted to the gravimetric geoidal height by adding a contribution from the Bouguer anomaly (Heiskanen and Moritz, 1967, pp. 327-328; Forsberg, 1984; Sjöberg, 2000):

$$N_{geoid} \approx \zeta + \frac{\Delta g_B}{\gamma} H \approx \zeta - \frac{2\pi G\rho}{\gamma} H^2 \qquad (8)$$

where Δg_B is Bouguer gravity anomaly (Fig. 2b). In the second identity in Eq. 8, error in the approximation using $\frac{2\pi G\rho}{\gamma} H^2$ is on the order of $\frac{\Delta g_F}{\gamma} H$, where Δg_F is free-air anomaly. This paper uses $\frac{\Delta g_B}{\gamma} H$ for the conversion.

The gravimetric geoid (and also the hybrid geoid) released in 2014 was computed on a 30"× 30" grid covering the area over 119.5°E–122.5°E and 21.5°N–25.5°N. In 2018, the coverage of the two geoid models was extended to 118°E–125°E and 21°N–27°N to include the islands Kinmen and Matzu near mainland China.

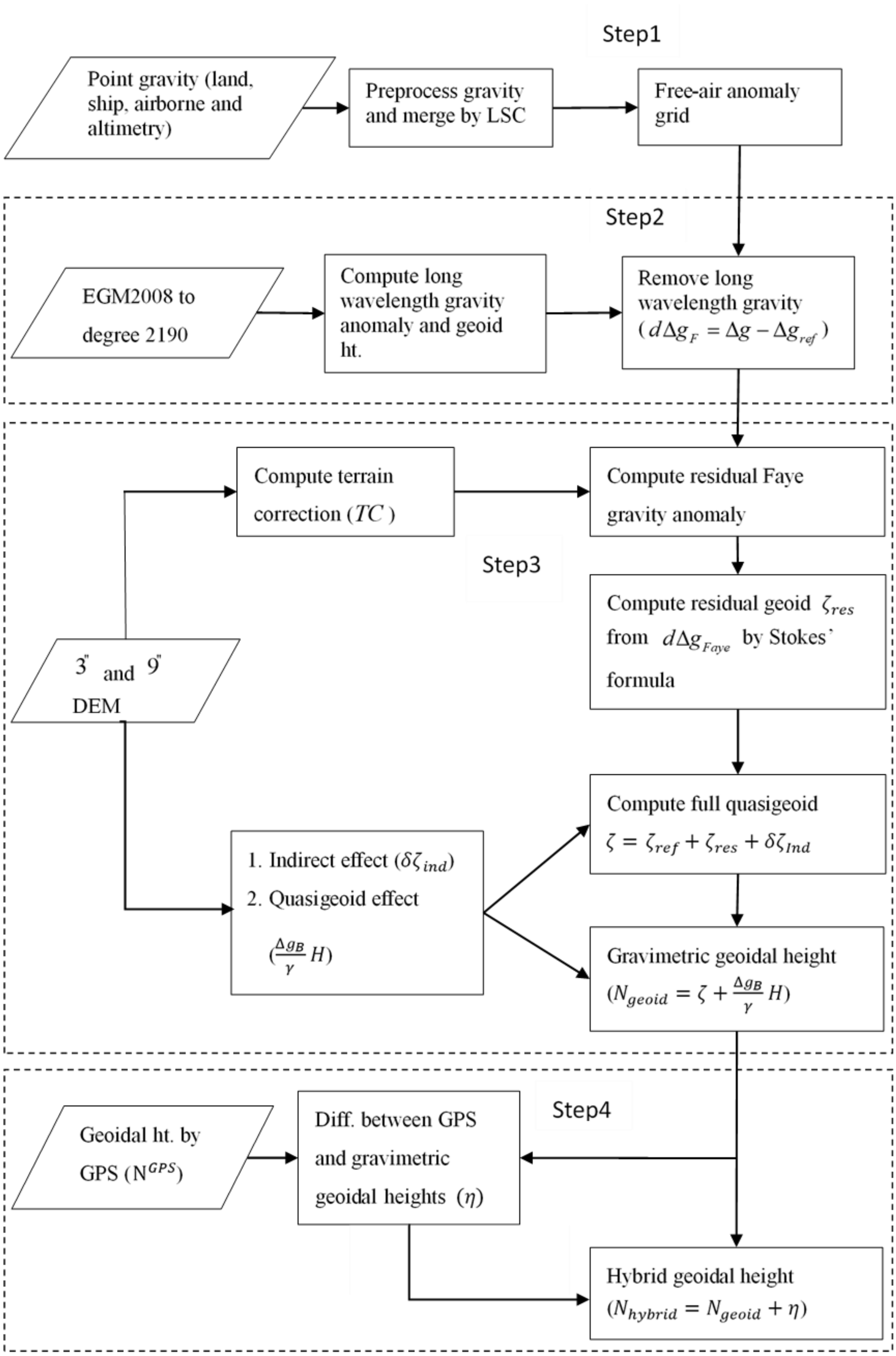

Fig. 4: The flow chart for geoid modeling in Taiwan. Steps 1-3 are for the gravimetric geoid, which is constrained to the observed geoid heights at the benchmarks in Fig. 3 in Step 4 to form the hybrid geoid.

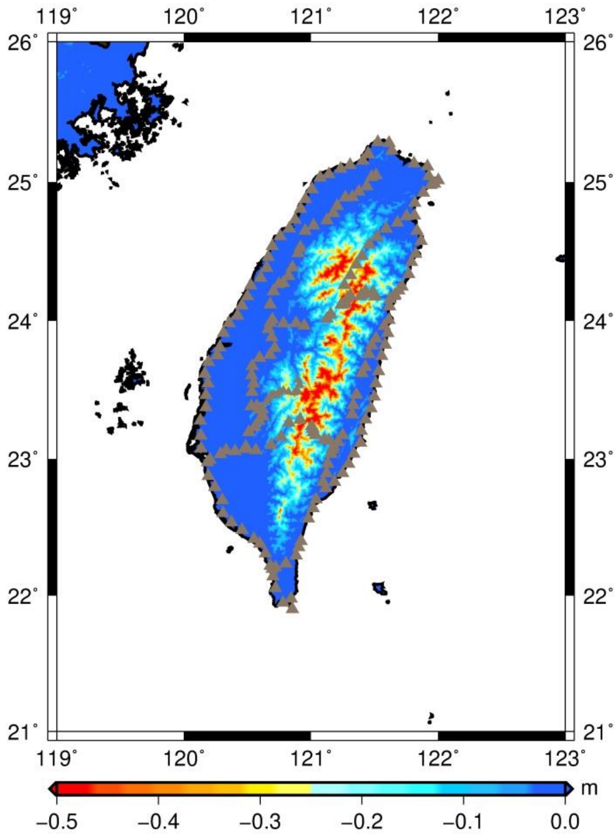

Fig. 5: Indirect effects according to Eq. 6. The gray triangles show the benchmarks where the geoid accuracy assessment is made (Section 4.1).

3.2 The hybrid geoid

The hybrid geoid is created in Step 4 (Fig. 4) by adding the "corrections" η to the gravimetric geoid heights. The gravimetric geoid model in Section 3.1 was derived solely from gravity data. The precision, accuracy and resolution of the gravimetric geoid model are highly dependent on the quality and spatial resolution of the gravity data. The use of a reference field (Eq. 1) and integration only over a limited cap (implied in Eq. 4), among other factors, can introduce long wavelength errors. In addition, orthometric heights based on a gravimetric geoid will not be compatible with the orthometric heights from leveling simply because the latter are defined in a conventional vertical datum based on one or more mean sea levels, rather than the geoid.

This compatibility with conventional orthometric heights and the long wavelength errors in the gravimetric geoid can be reduced by merging the GPS-observed geoid heights (Fig. 3c) into the gravimetric geoid. The observed geoid heights can also improve the spatial resolution of the gravimetric geoid by filling gaps where no gravity data are available for geoid modeling (Milbert, 1995). In this paper, we use the following procedure to create the hybrid geoid:

(1) Compute the differences between GPS-levelling-observed geoid heights (Fig. 3a–c) and the gravimetric geoid heights.

(2) Construct a 30" × 30" grid from the differences (herein called a geoid "correction" grid) using the "surface" command of GMT (Wessel et al., 2013), which is based on the minimum curvature principle.

(3) Add the geoid "correction" grid (η) to the grid of the gravimetric geoid to obtain the hybrid geoid model (on a 30"× 30" grid).

When constructing the "correction" grid in the second step by the minimum curvature method, it is important that (a) the geoid corrections will not undergo large oscillations in regions with sparse observed geoid heights (Fig. 3, especially mountainous areas), and (2) the geoid corrections will not be too smooth; this is to ensure that the hybrid geoid model captures high-frequency geoidal variations. To meet these two considerations, we experimented with different tension factors in "surface". We decided that a tension factor of 0.25 is the optimal choice, which is also recommended by the authors of GMT for interpolating potential field data.

Figures 6a, b and c show the hybrid geoid, its difference with the EMG2008 geoid (full use of all coefficients) and with the gravimetric geoid, respectively. Large hybrid-EGM2008 geoidal differences occur in the mountainous areas, because here the EGM2008 geoid uses only gravity anomalies on the first-order benchmarks (Fig. 3a;

the first author is the data provider). The hybrid-gravimetric geoid differences show that there are long wavelength differences between the two models. In the western coastal area (Fig. 6c), the differences reach 0.1–0.2 m; this area is the most populated region of Taiwan. In the mountainous regions, we also see differences up to about 0.3-0.4 m between the hybrid geoid and gravimetric geoid. More discussions on the geoidal differences are presented in Section 5.3 for LiDAR mapping.

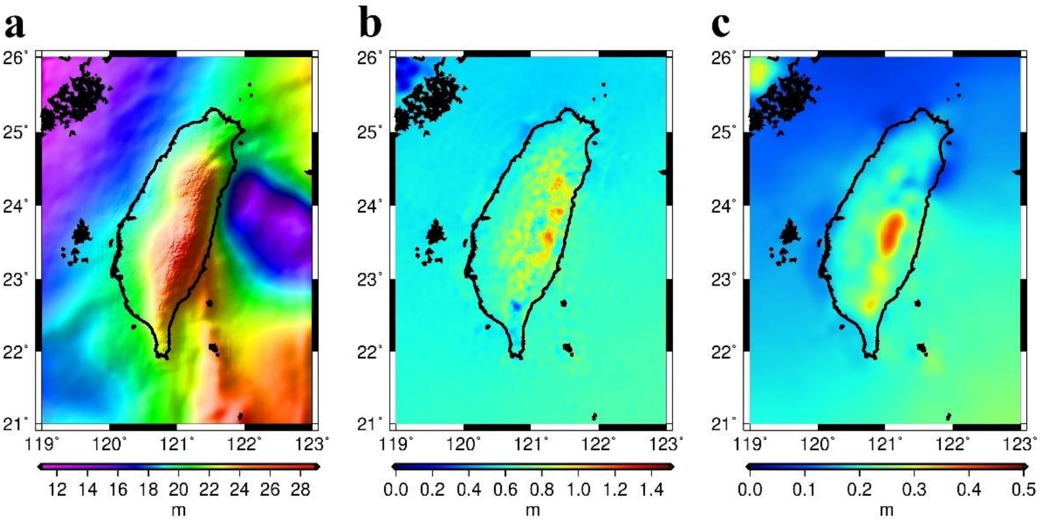

Fig. 6: (a) The hybrid geoid model of Taiwan, (b) its difference with the geoid model from EGM2008 to degree 2190 (c) its difference with the gravimetric geoid.

4. Precision assessment and error model

4.1 Precision assessment

In our geoid model assessments, the differences between the observed geoid heights and those interpolated from the gridded geoid model at these observation points were computed, followed by computations of the statistics of the differences. To ensure the assessment result is correct, we used only the ellipsoidal heights on the 214 first-order benchmarks along 14 leveling routes (Fig. 3b), where the GPS observation sessions were longer than 12 hours and the orthometric heights at the mm level were determined by precision leveling. We also used the ellipsoidal heights at 52 eGNSS continuous stations (Fig. 3c) in the assessments. At the 52 eGNSS stations, the orthometric heights were determined using the same level of precision as the one used for the first-order leveling benchmarks.

Table 4 shows the statistics of the differences between the observed and modeled (gravimetric) geoid heights. On the 214 benchmarks, the geoidal differences range from 0.8 cm to 39.7 cm, with a mean of 21.9 cm and a standard deviation of ±7.9 cm. The mean differences along the 14 leveling routes vary from 11.0 cm to 33.1 cm. The relatively large standard deviations along several routes are partially caused by the relatively low geoid precision resulting from sparse gravity data coverage, especially in high mountainous areas. At the 52 eGNSS stations (Fig. 3c), the point differences range from 2.6 cm to 29.0 cm, and the mean and the standard deviation of the differences are 20.0 cm and ±6.5 cm, respectively.

Table 5 shows the statistics of the differences between the observed and the hybrid geoid heights (only on the 214 benchmarks as Table 4). All the observed geoidal heights (Fig. 3a-c) have been blended into the hybrid geoidal model, thus creating correlations between the observed and the hybrid geoidal heights. However, it is noted that the minimum curvature method of blending (Section 3.2) will not result in a hybrid geoid model that reproduces the observed geoidal heights. On the 214 benchmarks, the differences range from -22.3 cm to 5.7 cm. As expected, the standard deviations and the mean values of the differences along the 14 routes are smaller than those from the gravimetric geoid. The overall mean difference and standard deviation (214 benchmarks) are -0.9 cm and ±3.6 cm, respectively. At the 52 eGNSS stations, the mean difference decreases from 20.0 cm (gravimetric geoid) to 0.0 cm (hybrid geoid), and the standard deviation from ±6.5 cm (gravimetric) to ±5.1 cm (hybrid). The point differences (52 stations, hybrid) now range from -9.7 cm to 8.6 cm, again a substantial reduction in the geoid differences compared to the case of the gravimetric-only geoid model.

Table 4: Statisctics of the differences between observed and gravimetric geoid heights (unit: cm)

Route	Min	Max	Mean	Std. dev
North[a]	9.6	19.1	14.1	2.9
Central	2.0	19.0	11.0	6.1
South	27.6	39.7	33.1	4.6
East	24.4	37.0	29.9	4.0
Tai3	18.2	28.9	24.4	2.5
Tai9	13.1	29.5	25.0	4.3
Tai18	10.9	23.0	17.0	3.4
SW	7.1	28.3	18.5	6.5
NW	0.8	19.0	13.2	4.2
24hr_Mountain	5.3	23.2	13.1	5.8
24hr_Ecoast	4.6	36.2	23.7	7.6
12hr_Tai3	21.7	32.9	26.4	3.0
12hr_Tai8	12.1	36.2	26.9	7.8
12hr_Tai20	11.6	37.3	21.9	7.9
All benchmarks	0.8	39.7	21.9	7.9
eGNSS[b]	2.6	29.0	20.0	6.5

[a]The route names are shown in Fig. 3b.

[b] The stations are shown in Fig. 3c

Table 5: Statisctics of the differences between observed and hybrid geoid heights (unit: cm)

Route	Min	Max	Mean	Std. dev
North	-2.2	3.4	-0.4	1.8
Central	-21.0	-2.1	-9.2	7.3
South	2.3	5.7	3.9	1.2
East	-5.9	-0.2	-2.5	1.8
Tai3	-0.2	5.1	1.2	1.2
Tai9	-3.2	4.1	0.8	1.9
Tai18	-8.4	-0.1	-3.8	2.1
SW	-4.4	3.3	-0.3	1.8
NW	-6.5	2.9	-0.7	2.2
24hr_mountain	-22.3	-0.3	-5.1	6.5
24hr_Ecoast	-8.0	2.9	-0.4	2.3
12hr_Tai3	-3.5	2.4	-0.8	1.2
12hr_Tai8	-5.4	5.1	0.0	3.0
12hr_Tai20	-2.1	3.2	-0.3	1.5
All benchmarks	-22.3	5.7	-0.9	3.6
eGNSS	-9.7	8.6	0.0	5.1

4.2 Formal errors in the gravimetric geoid model using least-squares collocation

The paper uses the theory of least-squares collocation (LSC) to estimate the formal errors of the Taiwan gravimetric geoid using the gravity data and the geoid differences in Tables 4 and 5, and those not used in the two tables (Fig. 3a and c). This is to answer a frequentlly asked question of geoid users: how precise is a given geoid model? This same question is addressed in the recent geoid models of Australia (Featherstone et al., 2018), which provides grid-wise error estimates propagated from the uncertanties in the EGM2008 model, gravity anomalies and planar terrain corrections. First, Figs. 7a and b show the differences between the observed and modeled geoid heights at all the benchmarks in Fig. 3. Figure 7a shows that the mean difference for the gravimetric geoid is about 20 cm (observed minus modeled values; see Tables 4 and 5), which is reduced to almost zero for the hybrid geoid (Fig. 7b).

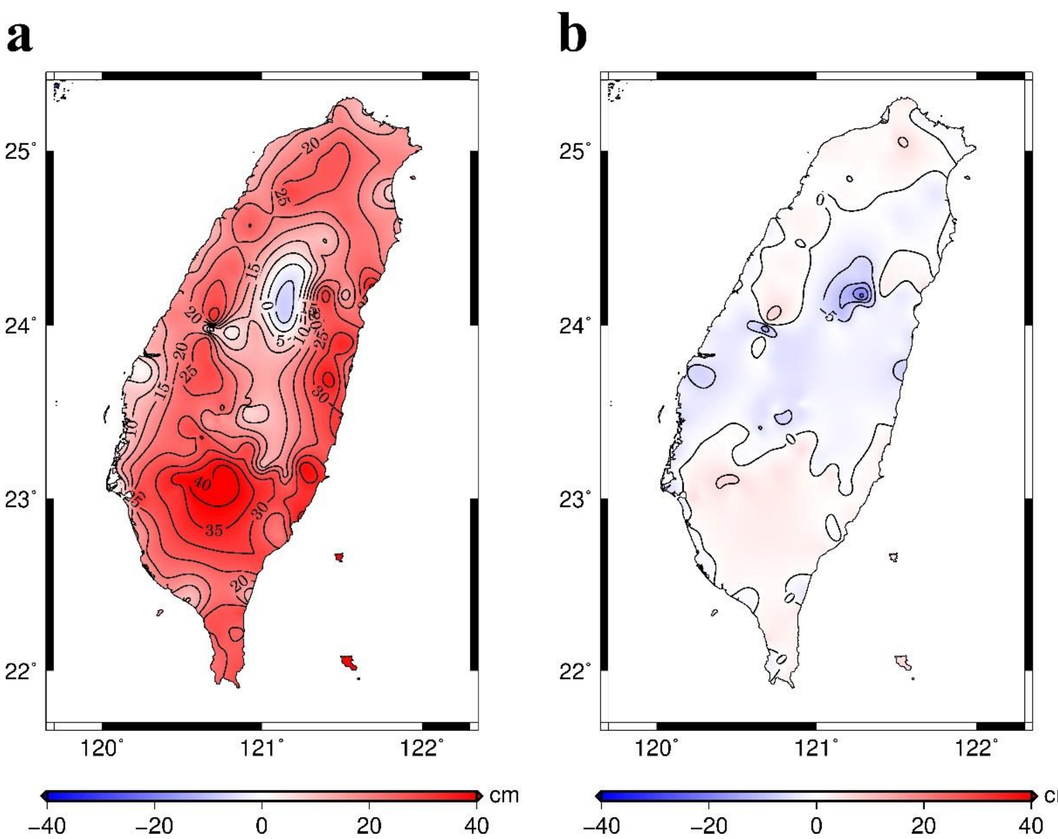

Fig. 7: Differences between the gravimetric geoid and the hybrid geoid, which are computed from (a) the differences between the observed geoidal heights and those from gravimetric geoid and (b), same but from the hybrid geoid at the benchmarks in Fig. 3a-c.

To estimate the formal errors of the gravimetric geoid using LSC, first we express the covariance function of residual gravity anomaly into a series of Legendre polynomials (Tscherning and Rapp, 1974):

$$C_{\Delta g \Delta g}(P,Q) = \sum_{n=2}^{n_{\max}} \delta \mathrm{C}_n \, s^{n+2} P_n(\cos\psi_{PQ}) + \sum_{n=n_{\max}+1}^{\infty} \mathrm{C}_n \, s^{n+2} P_n(\cos\psi_{PQ}) \tag{9}$$

where $n_{\max}$ is the maximum degree of the global gravity model (EGM2008 in this paper), P_n is the Legendre polynomial of degree n, $\delta \mathrm{C}_n$ is the error degree variance and C_n is the modeled signal degree variance (Model 4, Tscherning and Rapp, 1974).

The needed covariance functions can be derived from the law of covariance propagation and the detail has been given in Tscherning and Rapp (1974). Each of the gridded values in the gravimetric geoid model receives a formal error estimated as follows. The error variance of geoidal undulation at a grid point is computed by LSC as

$$\sigma_N^2 = \alpha[c_{NN}(0) - \mathbf{C}_{N\Delta\mathbf{g}}(\mathbf{C}_{\Delta\mathbf{g}\Delta\mathbf{g}} + \frac{1}{\alpha}\mathbf{D}_{\Delta\mathbf{g}})^{-1}\mathbf{C}_{N\Delta\mathbf{g}}^{\mathbf{T}}] \tag{10}$$

where $c_{NN}(0)$ is the geoid variance (a scalar), $\mathbf{C}_{N\Delta\mathbf{g}}$ is a row vector containing the covariance values of geoid undualtion-gravity anomaly, and $\mathbf{C}_{\Delta\mathbf{g}\Delta\mathbf{g}}$ and $\mathbf{D}_{\Delta\mathbf{g}}$ are matrices containing the covariance values of gravity anomaly-gravity anomaly and noise variance (squared standard error gravity measurement;Table 1), and α is the ratio between the variance of the residual gravity anomalies within the data selection window (see below) and the model variance ($\psi_{PQ} = 0$ in Eq. 9). The data for constructing the covariance matrices in Eq. 10 are from the original gravity data shown in Fig. 1, and the window of data selection is $10' \times 10'$ centered at a given grid point. In addition, the gridded formal geoid errors (squared root of σ_N^2) are scaled by a factor computed by

$$S = \frac{\bar{\sigma}_N^2}{\bar{\sigma}_e^2} \tag{11}$$

where $\bar{\sigma}_N^2$ is the variance of the differences between the gravimetric geoid heights and the observed geoid heights at the benchmarks in Table 4, and $\bar{\sigma}_e^2$ is the mean of the variances (from Eq. 10) over these benchmarks. S can be regarded as the ratio between the external variance ($\bar{\sigma}_N^2$) and the internal variance $\bar{\sigma}_e^2$. The result shows that S= 3.3368 (meaning all the internal errors from Eq. 10 are multiplied by about 1.8).

Figure 8 shows that the formal errors (scaled standard errors) of the gravimetric geoid model are roughly positively correlated with the free-air gravity anomalies (Fig. 2). The errors are relatively small in the western coastal plains. The errors in the mountainous areas are relatively large because (1) the gravity field here is rough, causing large scale factors (α) in Eq. 10, and (2) the land gravity data points here are sparse (Fig. 1a) and the gravity information is mostly from the airborne gravity values, which have relatively large standard errors compared to ground-based gravimeter observations.

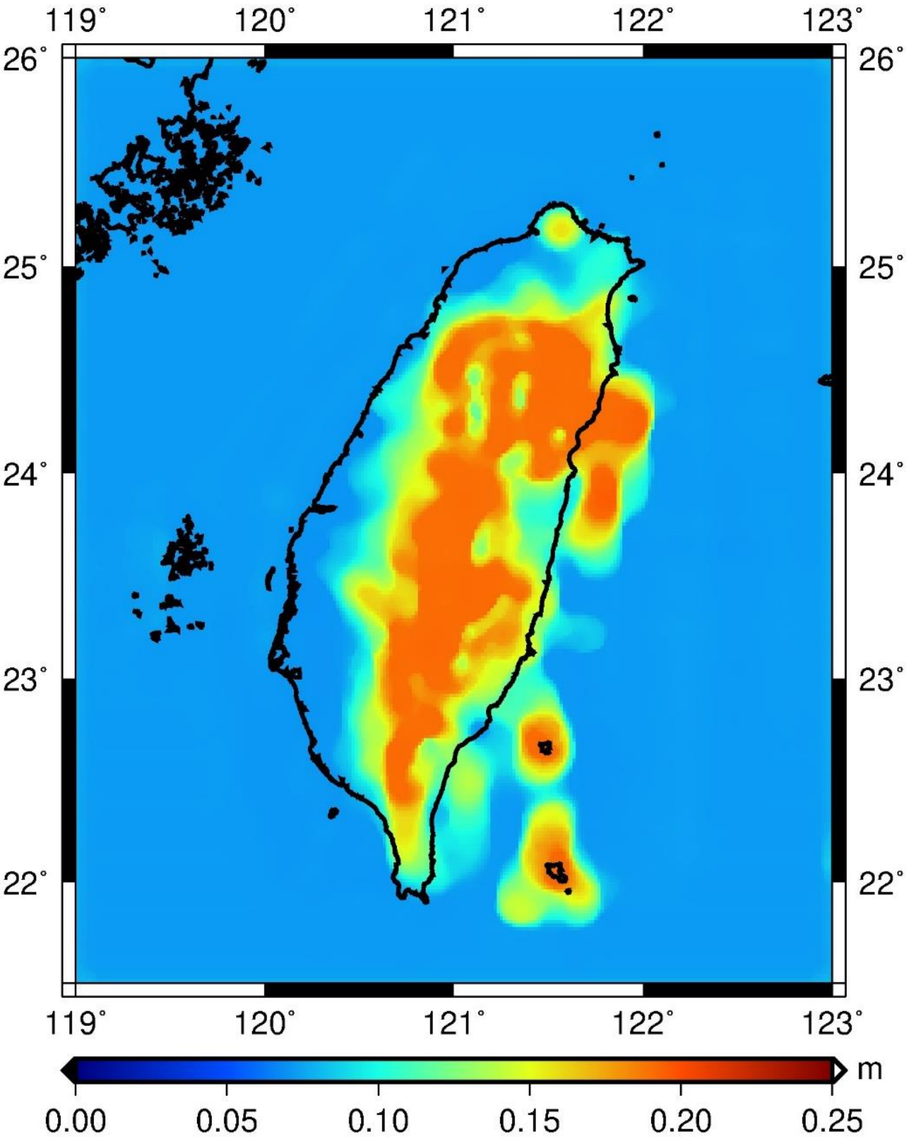

Fig. 8: Scaled standard errors of the gravimetric geoid model

5. Geoid applications

5.1 Height modernization and vertical land motion

Height modernization uses GNSS to determine orthometric heights by differencing ellipsoidal and geoid heights. The key to this process is a high-precision geoid model. In this modern method, the orthometric height of a new benchmark, H_B, is determined by (e.g., Zilkoski et al., 2008)

$$H_B = H_R + (\Delta h_{BR} - \Delta N_{BR}) \tag{12}$$

where H_R is the orthometric height at a reference station, Δh_{BR} and ΔN_{BR} are the differences in ellipsoidal height and in geoid height between the reference station and the new benchmark. One can expect that the errors in Δh_{BR} and ΔN_{BR} will decrease with the distance between the reference station and the benchmark (cf. Brown et al., 2018). In Eq. 12, the error associated with H_R is at about mm level, while error of ΔN_{BR} is at few cm level and error of Δh_{BR} can be as low as 1–2 cm in Taiwan (see below). Therefore, the error of H_B is governed by ΔN_{BR} (see the size of errors in Fig. 7a, b). In addition, differencing Δh_{BR} and ΔN_{BR} can reduce common-mode errors in GPS-derived ellipsoidal heights and the biases in the geoid model, especially when the baseline between B and R is short (Kearsley, 1988). Also, as shown in Table 4, the gravimetric geoid can result in larger mean difference than those from a hybrid geoid. Thus, for ellipsoidal to orthometric height conversion, a gravimetric geoid can benefit from the height differencing more than a hybrid geoid. The errors arising from the use of ΔN_{BR} have been discussed in many studies, e.g., Featherstone et al. (2001) and Saleh et al, (2013).

In Taiwan, real-time three-dimensional positioning is implemented using a network of 76 eGNSS stations (Fig. 9) and the technique of real-time kinematic virtual base stations (RTK-VBS) that minimizes the distance between a virtual reference station and a roving (new) station (e.g., Hu et al., 2003; Retscher, 2002). At the 76 eGNSS stations (including the 52 stations in Fig. 3c), the orthometric heights under the TWVD2001 vertical system have been measured using precision leveling and can be used for real-time orthometric heighting.

The eGNSS system of Taiwan's National Land Survey Center (NLSC) has been operational since 2004. It has been shown that eGNSS can achieve 2.5 cm in the three-dimensional positions for roving stations, suggesting the precision in the vertical component (ellipsoidal height) can reach 2 cm (Yeh et al., 2012). However, before the release of the geoid model in this paper, the eGNSS has not been officially used to determine orthometric heights in the way new horizontal positions are determined using RTK-VBS. The concern largely comes from the uncertainty of geoid models.

In collaboration with the NLSC of Taiwan, we assessed the precision of the hybrid geoid model for height modernization using eGNSS on 86 benchmarks (Fig. 10) at Hengchun Peninsula, where the observed geoid heights are not used in constructing the hybrid geoid.

Because a VBS created by eGNSS does not have an observed geoid height (thus they cannot provide real-time orthometric heighting unless the system is modified), we use the following post-processing procedure to determine the orthometric heights at any of the 86 benchmarks (Fig. 10) as follows:

(1) Use the RTK-VBS method to compute the latitude, longitude and ellipsoidal height of the benchmark.

(2) Compute the ellipsoidal height difference and the geoidal height difference (from the hybrid geoid) between the benchmark and the nearest eGNSS station, and then compute the orthometric height (GNSS-derived orthometric height) using Eq. (12).

Table 6 shows the statistics of the differences between the observed orthometric heights (by precision leveling) and the GNSS-geoid-derived orthometric heights at the 86 benchmarks. In Table 6, we also show the statistics excluding 7 benchmarks where large differences (those >15 cm in magnitude) exist. Such relatively large differences occur in areas with rapid vertical land motion, and in the western side of the Hengchun Peninsula (Fig. 10) where the geoid slopes are larger than elsewhere, creating larger uncertainties in the interpolated geoid heights. In addition, errors in the ellipsoidal heights from the RTK-VBS can also contribute to the large differences at the 7 benchmarks. If only the 79 benchmarks are considered, the RMS difference is 5.3 cm, which is roughly the accuracy of a GNSS-derived orthometric height one would expect using the RTK-VBS ellipsoidal height and interpolated geoidal height from the hybrid geoid.

Here we show a somewhat unexpected application of the hybrid geoid in GNSS heighting. Because the orthometric heights from our hybrid geoid model are in the vertical datum of Taiwan (TWVD2001), we can compare the GNSS-derived orthometric heights with those from precision leveling to determine vertical land motion. In 2013, NLSC collected GPS data at 408 benchmarks, as shown in Fig. 11. The GPS data are used to construct third-order GPS control networks in Taiwan. The precisions of the ellipsoidal heights at these control points are better than one cm. In addition, most of these control points are near the stations that provide the geoid height differences for the construction of the hybrid geoid model (Section 3.2). As such, the geoidal heights from the hybrid geoid at these control points have been well constrained by the observed geoidal heights.

We differenced the GNSS-derived orthometric heights at the 408 benchmarks (from 2013) with the orthometric heights measured in 2007 (by precision leveling). The differences are shown in Fig. 11. The rates of vertical land motions can be computed using the ratios of height differences in Fig. 11 and the time spans of about 7 years (from 2007 to 2013). Figure 11 shows land subsidence in western coast areas, which have been reported in (e.g., Hung et al., 2011). In the central, mountainous region of Taiwan, the rates are mostly positive, and are the result of plate collision. Here the vertical rates can reach 4 cm/year. The height changes in Fig. 11 are consistent with those estimated by Ching et al. (2011) and can be used in an updated vertical deformation model of Taiwan. The above height change analysis shows the additional value of the hybrid geoid model in vertical land motion modeling.

Table 6: Statistics of differences (in m) between the observed (by leveling) orthometric heights and GNSS-derived orthometric heights at 86 benchmarks

No of Benchmarks	Mean	Std dev	RMS
86 (all)	0.000	0.073	0.073
79 (ex. diff> 15 cm)	0.007	0.053	0.053

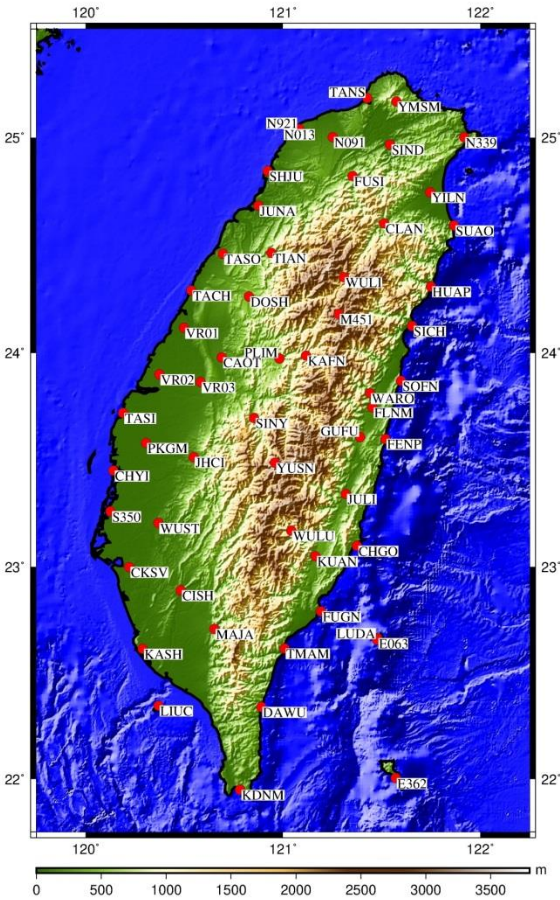

Fig. 9: The 56 GNSS stations in the eGNSS network for height modernization and RTK-VBS positioning (including the 52 stations in Fig. 3c for the hybrid geoid model).

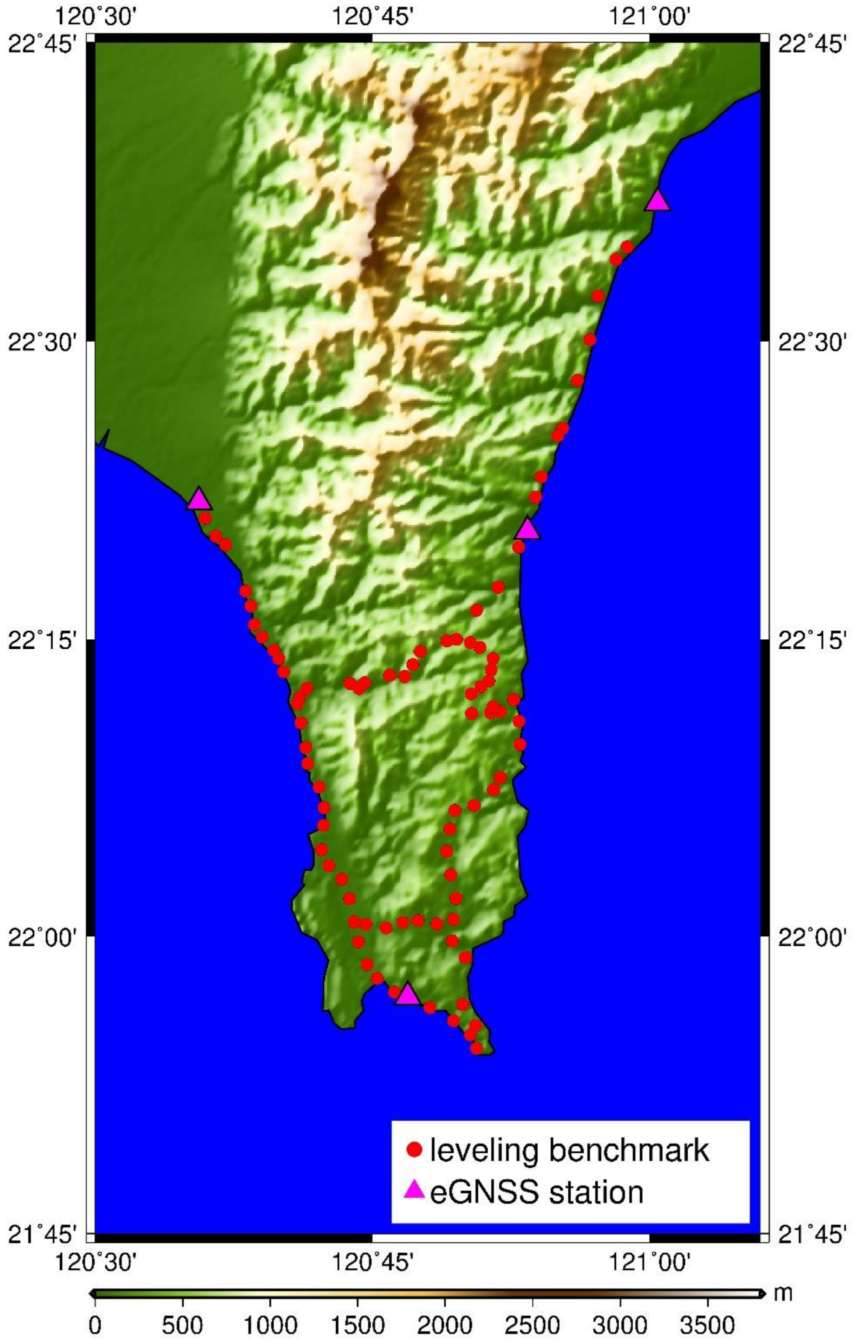

Fig. 10: Benchmarks (circles) at Hengchun Peninsula where the accuracy of the hybrid geoid model is assessed for height modernization. Triangles represent the eGNSS stations in Fig. 7.

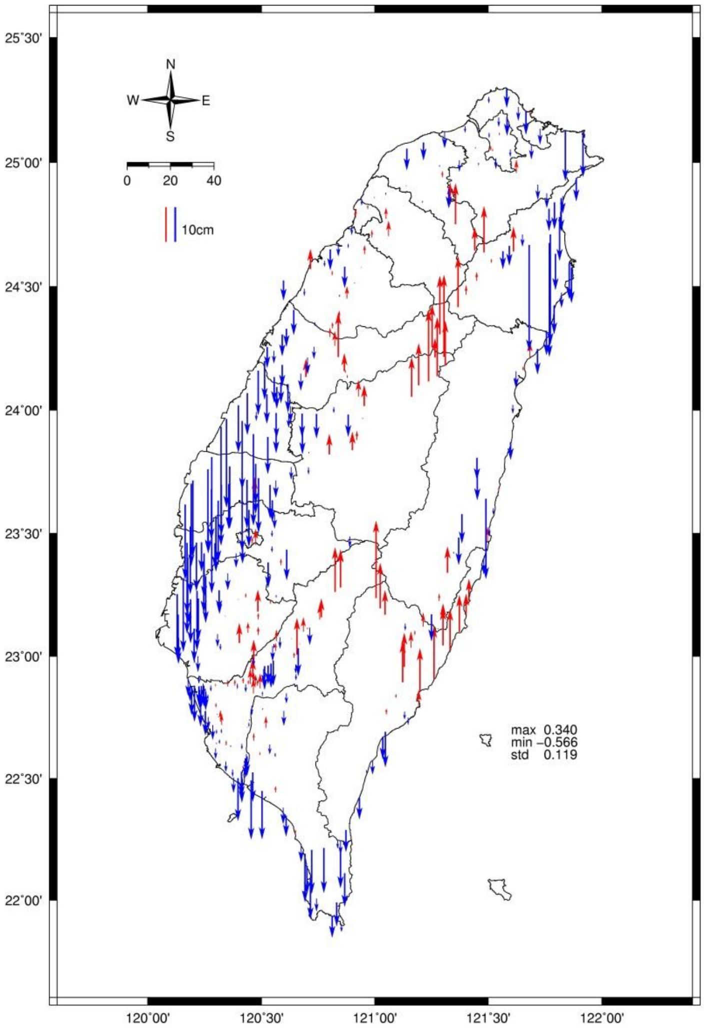

Fig. 11: Height changes at 408 third-order GPS control points derived from the differences between the orthometric heights in 2013 (from GPS and the hybrid geoid) and 2007 (from precision levelling). Blue vertical bars show land subsidence while red bars show uplift.

5.2 Cross-island vertical datum connection

The island of Taiwan uses a vertical datum for which the zero elevation is at the mean sea level of Keelung (KL) Harbour, located in northern Taiwan. The four offshore islands—Penghu, Ludao, Lanyu and Liuqiu (Fig. 1c), and islands not studied in this paper—use vertical datums whose zero elevations are the mean sea levels of the individual islands, derived from tidal records at their main tide gauges (Fig. 1d) over different time spans. The island of Taiwan and offshore islands are surrounded by one of the major western boundary currents, the Kuroshio Current, and oceanic currents that flow through the Taiwan Strait. In addition, the Kuroshio Current intrudes the waters off northern and southern Taiwan. This complicated ocean circulation system around Taiwan creates a MDT (also called sea surface topography, SST below) that causes large differences in the vertical datums between the island of Taiwan and its offshore islands (Hwang and Kao, 2002; see also Fig. 13 below). The MDT is the vertical separation between the mean sea surface and the geoid, and its role in creating vertical datum differences have been discussed in, e.g., Rapp and Balasubramania (1992), Featherstone and Filmer (2012), Gerlach and Rummel (2013), and Huang (2017).

As stated in Section 2.2, the ship gravity observations were collected within 50 km of the tide gauges defining the mean sea levels of the islands. The primary objective of these gravity measurements is to compute high-precision, high-resolution geoidal heights at the tide gauges, which can be used to determine the SST (MDT) value using (Fig. 12a)

$$\varsigma = h_{TG} - N_{TG} \tag{13}$$

where ς is SST, h_{TG} is the ellipsoidal height of the mean sea level near the tide gauge and N_{TG} is the geoidal height from the gravimetric geoid. Equation 13 suggests that the precision and potential systematic errors of ς are determined by those of h_{TG} and N_{TG}. In practice, to collect field data for determining ς in Eq. 13, the following procedure is used for each of the offshore islands and the island of Taiwan (Fig. 12c and 12d for Keelung and Ludao as two examples):

(1) Set up a temporary benchmark (P or K in Fig. 12a) with a GNSS open view, and it is as close as possible to the main tide gauge.

(2) Determine the orthometric height of the benchmark by precision leveling from the nearest benchmark in the first-order vertical control network of Taiwan or an offshore island (Fig. 6). Note: the orthometric height is in the local vertical datum.

(3) Collect GPS data for 48 hours at the benchmark (P or K) to compute the benchmark's ellipsoidal height.

To avoid potential long wavelength errors in the gravimetric geoid, this paper determines the relative MDT values between the main island of Taiwan and the four offshore islands using the geodetic method below. The difference in MDT between an island P and the island of Taiwan (K, standing for Keelung) is

$$\Delta\varsigma_{KP} = (h_P - H_P - N_P) - (h_K - H_K - N_K) = SST_P - SST_K \qquad (14)$$

where

h_P and h_K: the ellipsoidal heights of P and K

H_P and H_K: the local orthometric heights of P and K (local because they are based on the zero elevations at MSL_P and MSL_K in Fig. 12a)

$h_P - H_P$ and $h_K - H_K$: the ellipsoidal heights of the mean sea levels near P and K (Fig. 12a)

N_P and N_K: the geoid heights at P and K

Table 7 shows the SST differences from the geodetic method. In Table 7, we estimate the standard error of $\Delta\varsigma_{KP}$ by

$$\sigma_{\Delta\varsigma_{KP}} = \sqrt{\sigma^2_{\Delta h_{KP}} + \sigma^2_{\Delta H_{KP}} + \sigma^2_{\Delta N_{KP}}} \qquad (15)$$

where $\sigma_{\Delta h_{KP}}$, $\sigma_{\Delta H_{KP}}$ and $\sigma_{\Delta N_{KP}}$ are the standard errors of the differences in ellipsoidal height, local orthometric height and geoidal height, which are derived from the following error estimates: formal error of vertical component in the GPS positioning (48-hour GPS sessions for all tide gauges), $\sigma_{\Delta H_{KP}} = 0$ cm (error in precision leveling is negligible compared to errors in GNSS and the gravimetric geoid model), and $\sigma_{\Delta N_{KP}} = 2$ cm (the mean precision of the gravimetric geoid in coastal areas of Taiwan).

For comparison with the geodetic MDT, we also determined the MDT differences by the oceanographic method and the altimetric method. In the oceanographic method, we obtained the mean MDT values on a 0.125°×0.125° grid over 1982–2005 (24 years) from the model output of the Princeton Ocean Model (POM) in the western Pacific. The model set up of POM is described in Wu et al. (2008). Figure 13 shows the POM-derived relative MDT values. The oceanographic method is affected by the input data and boundary conditions to the POM model, and the spatial resolution of the model output. The oceanographic method provides an independent estimate of MDT values to assess the results from the geodetic method and the altimetric method. The MDT gradient east of Taiwan (Fig. 13) is largely the result of the oceanic gyre in the northern Pacific Ocean and the Kuroshio Current. The MDT field in Fig. 13 indicates relatively large MDT values over waters off the islands of Lanyu and Ludao.

The altimetric method determines MDT values by subtracting geoid heights in the oceans from mean surface heights from multiple altimeter missions. In this paper, we obtained two sets of geodetic MDT: (1) values from the DTU10 mean sea surface and MDT model (Andersen, 2010), and (2) values by subtracting EGM2008 geoid heights from the mean sea surface heights of DTU15 (from https://www.space.dtu.dk/english/research/scientific_data_and_models/global_mean_ sea_surface). Table 8 compares the relative MDT values from the geodetic, oceanographic and altimetric methods. Table 8 suggests that the relative MDT values at Penghu and Lanyu from the geodetic method are much larger than those from the oceanographic and altimetric methods (both DTU10 and DTU15). It has been reported by local civil engineers that drainage systems in the coastal area of Matzu (an offshore island not studied in this paper) were flooded by sea water because the measured orthometric heights (in the local vertical system) seems to be incorrect (NLSC, private communication, May 2019). That is, the physical location of MSL_P in Fig. 12a could be not at the mean sea level of the offshore island. This problem is explored below.

In Taiwan, the Central Weather Bureau (CWB) is the agency who used tidal records to define the physical locations of the mean sea levels around the five tide gauges in the 1990s. This is illustrated in Fig. 12b, in which “reference” is a marker (usually a red line) at the tide gauge facility. The vertical distance from this marker to the “mean sea surface” is defined by a number H_0 (this value was documented by CWB). For any island, including Taiwan, a tidal record is the height above this mean sea surface. On the other hand, the mean sea levels in Fig. 12a at K and P can be physically located by using their H_0 values and their markers. However, before 2017 there was no verification that if the current H_0 values really define the local mean sea levels at Penghu and Lanyu. Furthermore, in Fig. 12b, h_1 is the height difference between this marker and a tide gauge benchmark. The orthometric height of this benchmark is $H_{TG} = H_0 - h_1$. By differential leveling, the height H_{TG} can be propagated to the heights of the benchmarks in the vertical control network of an offshore island.

We explore the potential problem with the physical location of local mean level by using a sensor to measure instantaneous sea level, T_m, relative to the level of H_{TG} (Fig. 12b). The simultaneous tidal measurement is T_P (relative to the "reference" marker). The measurements of T_m and T_P should satisfy

$$H_{TG} - T_m = (H_{TG} + h_1) - T_P = H_0 - T_P \tag{16}$$

We carried out measurements of T_m around tide gauges near Keelung (Taiwan) and on the four islands (T_P are from the tidal records provided by CWB). Our result shows that the differences between $H_{TG} - T_m$ and $(H_{TG} + h_1) - T_P$ range from -1.2 cm to 7.5 cm. This suggests that there are no major problems with the current tidal records, potentially caused by incorrect relative positions defined by H_0, h_1 and H_{TG} at the five tide gauges.

Next, we investigate the potential MDT problem by computing the mean values of the tidal heights, whose origins (zero tidal heights) are the positions defined by the current H_0 values (relative to "mean sea surface" in Fig. 12b). The mean values at Penghu and Lanyu are -41.7 cm and -54.1 cm and a few cm at Keelung, Ludao and Liuqiu tide gauges. This means that the actual local mean sea levels at Penghu and Lanyu are 41.7 cm and 54.1 cm below the positions defined by the current H_0 values and tidal heights; this means the current level MSL_P in Fig. 12a (for Penghu and Lanyu) should be lowered by 41.7 cm and 54.1 cm, and all the orthometric heights in the vertical network of these two islands should be increased by these two values.

The incorrect physical locations of the mean sea levels at Penghu and Lanyu also explain the large relative (and incorrect) MDT values of these two islands (Table 7). If we remove the offset values of 41.7 cm at Penghu and 54.1 cm at Lanyu, the resulting MDT values are 2.4 cm (=44.1-41.7 cm) and 51.7c m (=105.8-54.1 cm), respectively, which are more consistent with the MDT values from the other three methods in Table 8. The examples at Penghu and Lanyu show that the gravimetric geoid can verify whether an existing vertical datum of an offshore island is based on a correct mean sea level. On the other hand, if the vertical datums of these two islands are correctly placed at their local mean sea levels, the gravimetric geoid can be used to determine a reliable MDT difference between the main island of Taiwan and each of the two islands for a proper vertical datum connection.

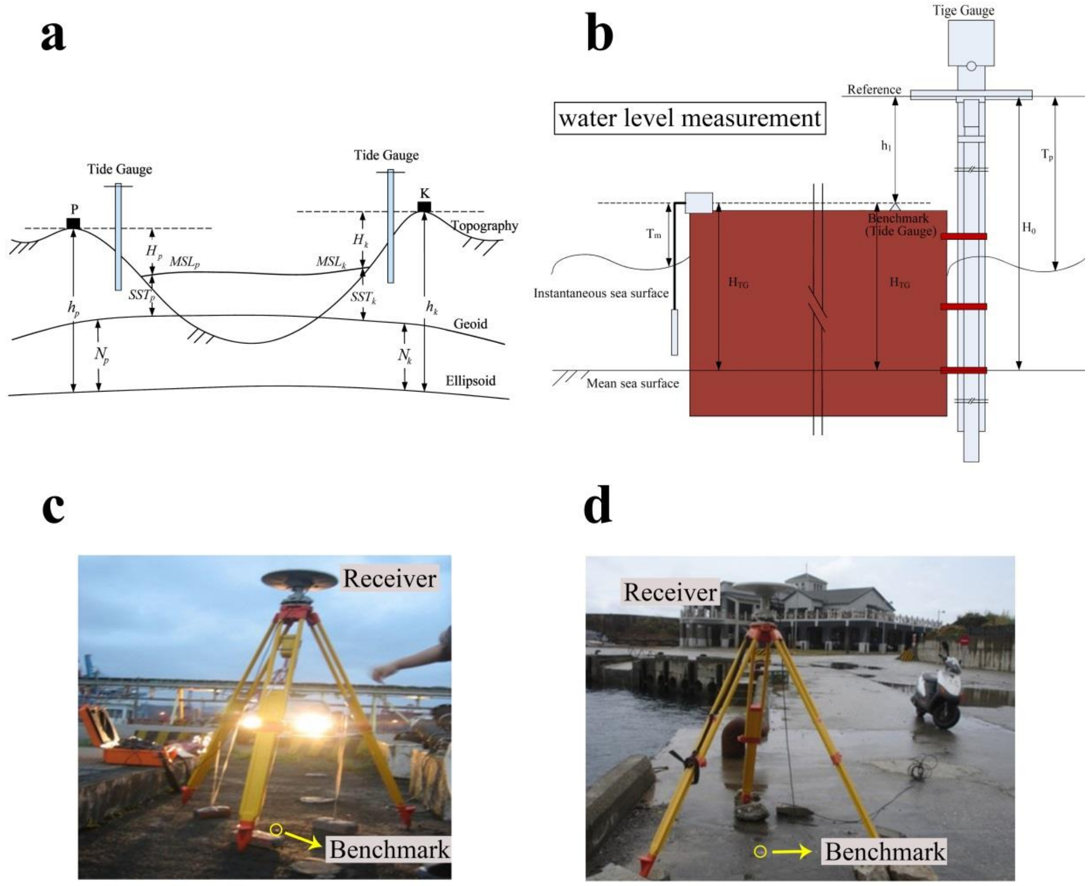

Fig. 12: (a) The geodetic method for determining vertical datum differences (relative SST values) between two islands (see the text for the symbols) (b) the H_0 value. ($H_0 = H_{TG} + h_1$) that defines the mean sea surface at a tide gauge; water level measurements are collected for calibrating tidal record errors (Eq. 13) (c) GPS field work at the benchmark near the tide gauge defining the mean sea level of Taiwan (Keelung Harbour) (d) same as (c), but on Ludao.

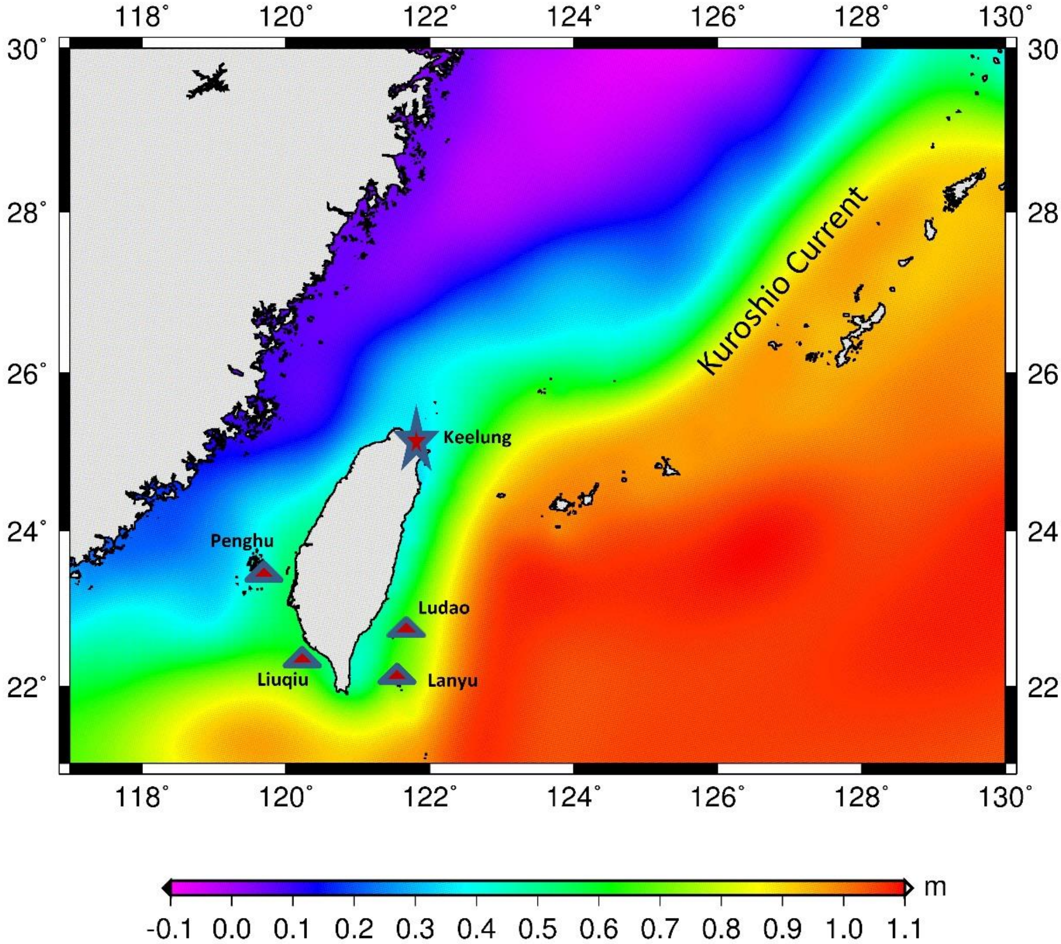

Fig. 13: The ocean's mean dynamic topography (MDT) around Taiwan obtained by averaging the MDT values over 1982-2005 from the POM model output of Wu et al. (2008), with the locations of the five tide gauge stations (star for Taiwan, and triangles for the rest).

Table 7: Vertical datum differences between Taiwan and four offshore islands using the geodetic method (unit: m)

	Δh	ΔN	ΔH_G	ΔH	Geodetic SST	Std err of SST
LQ-KL[a]	3.140	0.153	2.978[b]	2.732	0.246	0.021
LD-KL	6.633	3.878	2.745	2.241	0.504	0.023
LY-KL	10.977	4.192	6.773	5.715	1.058	0.022
PH-KL	-1.231	-2.014	0.777	0.336	0.441	0.024

[a] LQ MDT minus KL MDT

[b] $\Delta H_G = \Delta h - \Delta N$ (gravimetric geoid), ΔH = difference between two orthometric heights (defined in the island vertical datum and Taiwan vertical datum)

Table 8: Relative MDT between an offshore island and Taiwan from the geodetic method (Table 7) and three other sources (unit: m)

Island-Taiwan	Geodetic MDT	POM MDT	DTU10 MDT	DTU15 MDT
LQ-KL	0.246	0.212	0.279	0.298
LD-KL	0.504	0.284	0.441	0.267
LY-KL	1.058	0.332	0.443	0.489
PH-KL	0.441	0.044	0.072	0.096

5.3 LiDAR mapping of orthometric heights

In Taiwan, there were several LiDAR experimental measurement campaigns in the early 2000s, e.g., Shih et al. (2005), who reported a 5-cm precision in ellipsoidal heights in flat areas of Taiwan and precisions greater than 15 cm in mountainous areas. Since the early 2000s, LiDAR-derived high-resolution DEMs in Taiwan have been used to characterize faults in northern Taiwan (Chan et al., 2007), assess the effects of topography on seismic motions (Lee et al., 2009), and detect deep-seated faults in dense forests (Chen et al., 2015), among other applications.

After the disaster of Typhoon Morakot in August 2009 that caused several hundreds of deaths by landslides, the government of Taiwan decided to map the whole of Taiwan by LiDAR to identity locations prone to landslides and other geohazards. As a result, Taiwan has been surveyed with LiDAR by 2012 (Hou et al., 2014). The unique role of a geoid model in LiDAR mapping is for converting LiDAR ellipsoidal heights to orthometric heights. Earlier, there was no standard geoid model of Taiwan to serve this need. Thus, for the same LiDAR data, different geoid models can result in different DEMs. The current 5-m DEMs (orthometric heights) from LiDAR over Taiwan (Hou et al., 2014) are based on the hybrid geoid in this paper (area of Taiwan: 36,000 km^2). In 2015, 52578 frames of LiDAR-generated maps (containing orthometric heights and other spatial information) were requested by 40 organizations in Taiwan. In 2016, the numbers of requesting organizations and approved map frames increase to 79 and

78607, respectively, showing the increased importance of LiDAR-generated DEMs and the hybrid geoid.

Here we show an example of LiDAR mapping of orthometric heights and a potential problem with different geoid models in a low-lying, coastal area in southern Taiwan. Recent climate change has created extreme rainfalls that flooded several low-lying areas in southern Taiwan. For example, on August 23–25, 2018, southwestern Taiwan received a cumulative rainfall of 500 mm, which created major floods in several coastal townships of Chiayi and Tainan County. The floods were unprecedented and were not predicted by flood models. Since precise orthometric heights in low-lying areas are important for flood modeling (e.g., Merwade et al., 2008; Webster et al., 2004), the failures in predicting the floods over August 23–25, 2018 could be partly due to incorrect orthometric heights (from LiDAR measurements and an earlier geoid model) and partly due to neglecting elevation changes caused by the rapid land subsidence in these areas (subsiding rates up to 4.5 cm/year; Hung et al., 2011; Hung et al., 2018). In addition to rain, storm surges and high-tide water could also flood low-lying areas.

In a flood-prone area, the zero elevations from LiDAR-derived orthometric heights should be at about the local mean sea level for a realistic flood modeling. This can be achieved only when the hybrid geoid is used in the conversion from ellipsoidal heights to orthometric heights (see Section 3.2). As an example, Fig. 14a and b show the orthometric heights in two low-lying townships, Linbian and Jiadong, in Pingtung County (southern Taiwan), computed separately from LiDAR-derived ellipsoidal heights and the gravimetric and the hybrid geoid models. These two townships have long suffered from land subsidence and flooding. As shown in Fig. 14a and b, the zero elevations from the two geoid models are different. Figure 14c compares the areas of sub-zero elevations defined by the two geoid models. The orthometric heights from the gravimetric geoid are larger than those from the hybrid geoid by about 20 cm, resulting in underestimated flood-prone areas and a larger dry intertidal zone on the areas west of the seawalls. In contrast, the hybrid geoid results in more realistic sub-zero elevations and intertidal zone. If the zero elevation contours are used to assess the potential flood risk-prone areas in these townships, then two geoid models will lead to two different results and may affect governmental funds that are allocated to protect these lands.

A final note is given to the link between a geoid model and relative sea level rise in Taiwan (Hung et al., 2018), which is the relative motion of coastal land with respect to the sea. Because the rate of sea level rise is about 3 mm/year (Chen et al., 2013), a geoid model error of 20 cm (in the case of coastal Taiwan, Fig. 7a) corresponds to 70 years of sea level rise in mapping the risk of flooding using LiDAR-derived orthometric heights.

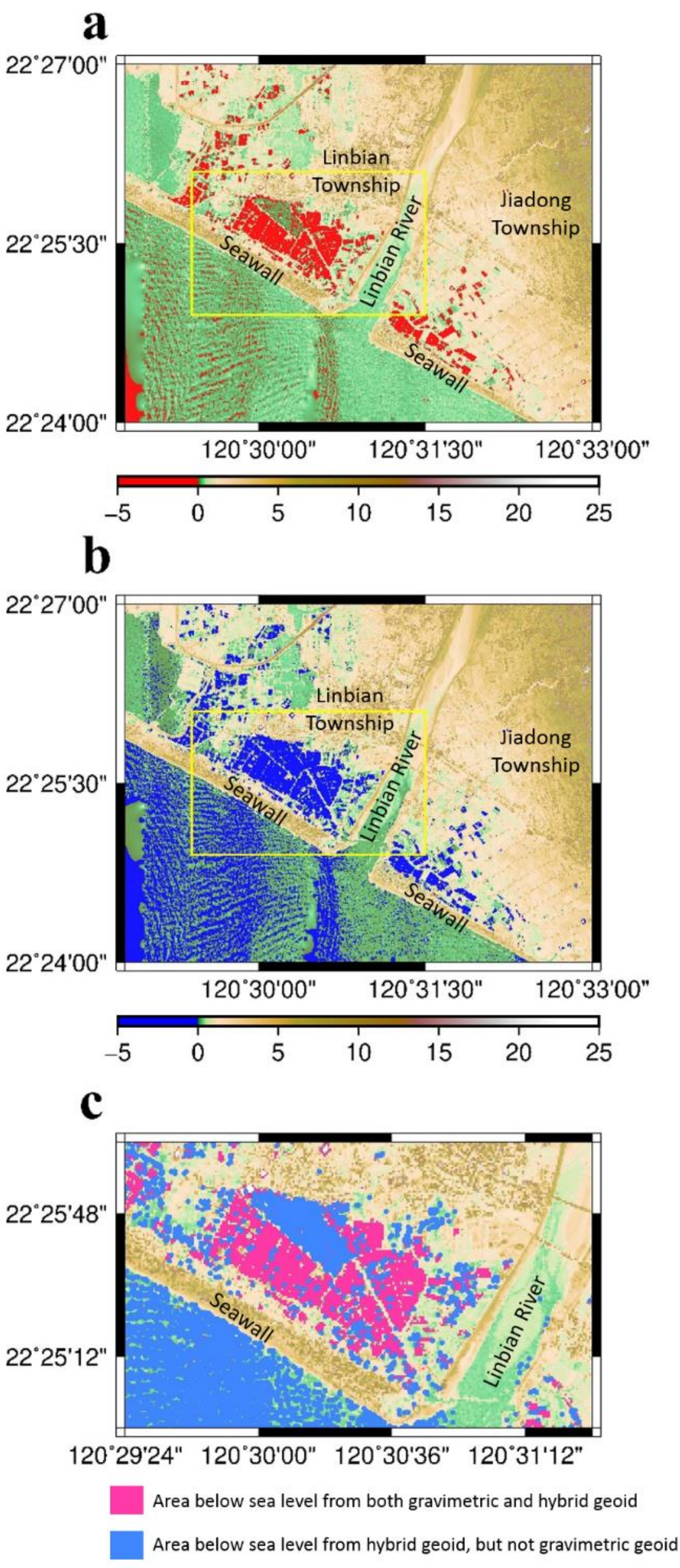
a
22°27'00"
22°25'30"
22°24'00"
120°30'00"
120°31'30"
120°33'00"
Linbian Township
Jiadong Township
Linbian River
Seawall
Seawall
–5
0
5
10
15
20
25
b
22°27'00"
22°25'30"
22°24'00"
120°30'00"
120°31'30"
120°33'00"
Linbian Township
Jiadong Township
Linbian River
Seawall
Seawall
–5
0
5
10
15
20
25
c
22°25'48"
22°25'12"
120°29'24"
120°30'00"
120°30'36"
120°31'12"
Seawall
Linbian River
Area below sea level from both gravimetric and hybrid geoid
Area below sea level from hybrid geoid, but not gravimetric geoid

854

Fig. 14: (a) Orthometric heights (color scale in meter) from LiDAR-derived ellipsoidal heights and the geoidal heights from the gravimetric geoid in a low-lying, flood-prone area of Pingtung County in southern Taiwan; sub-zero elevations are red-shaded, (b) same as (a), but from the hybrid geoid, sub-zero elevations are blue-shaded (c) comparison of sub-zero elevations in the yellow box (Linbian Township) of (a) and (b) from the two geoid models.

5.4 Economic and societal impacts of the geoid models

In addition to the three applications given in Section 5.1-5.3, numerous other applications of the geoid models were conducted that have economic and societal impacts. According to a survey by the Ministry of the Interior, Taiwan, more than 40 organizations (up to early 2019) in Taiwan have used the models in various applications. A sample study using the new Taiwan hybrid geoid developed in this paper is given by Li and Ning (2019).

These geoid applications include, but are not limited to (reported by Ministry of the Interior, Taiwan): GPS orthometric heights conducted by military units, topographic surveys for railway construction, production of rectified photogrammetric images, geophysical surveys over landslide-prone slopes, updates of digital maps, geodetic teaching, course work on integration of geospatial information, surveys of wastewater distribution and polluted soils, control surveys for the Taiwan High Speed Rail (THSR), construction work of landslide-hit areas, UAV (unmanned aerial vehicles) topographic measurements, height surveys of public pipelines, height surveys for high-voltage power towers and lines, aviation accident investigations, studies of creeping slopes, assessment of flood risks due to tsunamis, geothermal studies, drainage system designs, mapping fragile terrains, analysis of pandemic diseases, urban-look analysis, aviation safety and soil and water conservations.

6. Conclusion

In this paper, we constructed gravimetric-only and hybrid geoid models of Taiwan and show how such models can benefit works in height modernization, cross-island vertical datum connection and mapping orthometric heights with LiDAR. The high-resolution, high-quality gravity anomalies and the dense, accurate GPS-observed geoidal heights are two essential datasets for building these two geoid models, particularly over a rugged terrain like Taiwan, which is surrounded by oceans with rough gravity fields.

The gravimetric geoid, together with the GPS and the tidal records, helped us to identify errors of about 40–50 cm in the current vertical datums of Penghu and Lanyu islands offshore mainland Taiwan. That is, the gravimetric geoid model helps to improve the definition of an orthometric height at a benchmark related to a correct local mean sea level. This is important for engineering works that require accurate heights relative to sea level, such as construction of a coastal drainage system.

The hybrid geoid is used to directly determine cm-level orthometric heights under the conventional vertical datum of Taiwan (TWVD2001) from the eGNSS network. This practice will greatly improve the efficiency of land surveyor's orthometric heighting in Taiwan. An example in southern Taiwan shows that the hybrid geoid, rather than the gravimetric geoid, is needed for a more correct estimate of the flood-affected area from the LiDAR measurements because the hybrid geoid can yield orthometric heights relative to local mean sea level. This improvement of 20 cm for LiDAR mapping of flood-zone heights corresponds to 70 years of sea level rise. In view of the ever-advancing geodetic technologies, precise geoid modeling has become an increasingly important task for national mapping agencies around the world.

Acknowledgements

This study is funded by MOST, Taiwan, under grants 106-2221-E-009-133-MY3 and

107-2611-M-009-001, and Dept. of Land Administration, Ministry of the Interior, Taiwan, under the project "Gravity Datum Service" (2004 to present). We are grateful to the three anonymous reviewers, who provided very constructive comments to improve the quality of this paper.

Availability of data and material

The gravity, GPS and leveling data used in this paper are available at http://space.cv.nctu.edu.tw/publications/#data.

Author contributions: CH designed, wrote the paper and did the major computations, HJH and WHH did the geoid computations, WEF, CC, KWC and CYW helped with the theories and data analyses, MY, HC and WYS helped with the height modernization, CHH determined the mean dynamic topography and vertical datum differences, and JFH provided a geoid user analysis.

References

Andersen OB (2010). The DTU10 gravity field and mean sea surface second international symposium of the gravity field of the Earth (IGFS2). University of Alaska Fairbanks, Fairbanks, AK, USA.

Brown, NJ, McCubbine JC, Featherstone WE, Gowans N, Woods A, Baran I (2018). AUSGeoid2020 combined gravimetric–geometric model: location-specific uncertainties and baseline-length-dependent error decorrelation. Journal of Geodesy, 92(12), 1457-1465.

Chan YC, Chen YG, Shih TY, Huang C (2007). Characterizing the Hsincheng active fault in northern Taiwan using airborne LiDAR data: Detailed geomorphic features and their structural implications. Journal of Asian Earth Sciences, 31(3), 303-316.

Chen JL, Wilson CR, Tapley BD (2013). Contribution of ice sheet and mountain glacier melt to recent sea level rise. Nature Geoscience, 6(7), 549-552.

Chen KH, Yang M, Huang YT, Ching KE, Rau RJ (2011). Vertical displacement rate field of taiwan from geodetic levelling data 2000-2008. Survey Review.

Chen RF, Lin CW, Chen YH, He TC, Fei LY (2015). Detecting and characterizing active thrust fault and deep-seated landslides in dense forest areas of southern Taiwan using airborne LiDAR DEM. Remote Sensing, 7(11), 15443-15466.

Ching KE, Hsieh ML, Johnson KM, Chen KH, Rau RJ, Yang M (2011). Modern vertical deformation rates and mountain building in Taiwan from precise leveling and continuous GPS observations, 2000–2008. Journal of Geophysical research: solid earth, 116(B8).

Dach R, Lutz S, Walser P, Fridez P (2015) Bernese GNSS Software Version 5.2, Astronomical Institute. University of Bern, Switzerland.Denker H, Barriot JP, Barzaghi R, Fairhead D, Forsberg R, Ihde J, Kenyeres A, Marti U, Sarrailh M, Tziavos I (2009). The development of the European gravimetric geoid model EGG07. In Observing Our Changing Earth (pp. 177-185): Springer.

Featherstone WE, Filmer MS(2012). The north-south tilt in the Australian Height Datum is explained by the ocean's mean dynamic topography. Journal of Geophysical Research: Oceans, 117(C8).

Featherstone WE, Kirby JF, Kearsley AH, Gilliland JR, Johnston GM, Steed J, Forsberg R, Sideris M (2001). The AUSGeoid98 geoid model of Australia: data treatment, computations and comparisons with GPS-levelling data. Journal of Geodesy, 75(5-6), 313-330.

Featherstone WE, McCubbine JC, Brown NJ, Claessens SJ, Filmer MS, Kirby JF (2018). The first Australian gravimetric quasigeoid model with location-specific uncertainty estimates. Journal of Geodesy, 92(2), 149-168.

Forsberg R (1984). A study of terrain reductions, density anomalies and geophysical inversion methods in gravity field modelling (No. OSU/DGSS-355).

Gerlach C, Rummel R (2013). Global height system unification with GOCE: a simulation study on the indirect bias term in the GBVP approach. Journal of Geodesy, 87(1), 57-67.

Haagmans R (1993). Fast evaluation of convolution integrals on the sphere using 1D FFT and a comparison with existing methods of Stokes' integral. Manuscr. Geod., 18, 227-241.

Heiskanen WH, Moritz H (1967). Physical geodesy. San Francisco, WH Freeman [1967].

Hou CS, Fei LY, Chiu CL, Chen HJ, Hsieh YC, Hu JC, Lin CW (2014). Airborne LiDAR DEM and geohazards Applications. Journal of Photogrammetry and Remote Sensing, 18(2).

Hsiao YS, Hwang C(2010). Topography-assisted downward continuation of airborne gravity: an application for geoid determination in Taiwan. TAO: Terrestrial, Atmospheric and Oceanic Sciences, 21(4), 6.

Hu GR, Khoo HS, Goh PC, Law CL (2003). Development and assessment of GPS virtual reference stations for RTK positioning. Journal of Geodesy, 77(5-6), 292-302.

Huang J (2017). Determining coastal mean dynamic topography by geodetic methods. Geophysical Research Letters, 44(21), 11,125-111,128.

Huang J, Véronneau M (2013). Canadian gravimetric geoid model 2010. Journal of Geodesy, 87(8), 771-790.

Hung WC, Hwang C, Chen YA, Chang CP, Yen JY, Hooper A, Yang CY (2011). Surface deformation from persistent scatterers SAR interferometry and fusion with leveling data: A case study over the Choushui River Alluvial Fan, Taiwan. Remote sensing of environment, 115(4), 957-967.

Hung WC, Hwang C, Chen YA, Zhang L, Chen KH, Wei SH, Huang DR, Lin SH (2018). Land subsidence in Chiayi, Taiwan, from compaction well, leveling and alos/palsar: Aquaculture-induced relative sea level rise. Remote Sensing, 10(1), 40.

Hwang, C(1997). Analysis of some systematic errors affecting altimeter-derived sea surface gradient with application to geoid determination over Taiwan. Journal of Geodesy, 71(2), 113-130.

Hwang C (1998). Inverse Vening Meinesz formula and deflection-geoid formula: applications to the predictions of gravity and geoid over the South China Sea. Journal of Geodesy, 72(5), 304-312.

Hwang C, Guo J, Deng X, Hsu HY, Liu Y (2006). Coastal gravity anomalies from retracked Geosat/GM altimetry: improvement, limitation and the role of airborne gravity data. Journal of Geodesy, 80(4), 204-216.

Hwang C, Hsiao YS, Shih HC, Yang M, Chen KH, Forsberg R, Olesen AV (2007). Geodetic and geophysical results from a Taiwan airborne gravity survey: Data reduction and accuracy assessment. Journal of Geophysical research: solid earth, 112(B4).

Hwang C, Hsu HJ, Chang ET, Featherstone W, Tenzer R, Lien T, Hsiao YS, Shih HC, Jai PH (2014). New free-air and Bouguer gravity fields of Taiwan from multiple platforms and sensors. Tectonophysics, 611, 83-93.

Hwang C, Kao R (2002). TOPEX/POSEIDON-derived space–time variations of the Kuroshio Current: applications of a gravimetric geoid and wavelet analysis. Geophysical Journal International, 151(3), 835-847.

Hwang C, Shih HC, Hsiao YS, Huang CH (2012). Airborne gravity surveys over

Taiwan Island and Strait, Kuroshio Current and South China Sea: comparison of GPS and gravity accuracies at different flight altitudes. Marine Geodesy, 35(3), 287-305.

Hwang C, Wang CG, Hsiao YS (2003). Terrain correction computation using Gaussian quadrature. Computers & geosciences, 29(10), 1259-1268.

Johnson, B (2009). Noaa project to measure gravity aims to improve coastal monitoring. Science, 325 (5939), p. 378.

Kearsley A HW (1988). Tests on the recovery of precise geoid height differences from gravimetry. Journal of Geophysical Research: Solid Earth, 93(B6), 6559-6570.

LCR (2003). Instruction manual for Lacoste & Romberg model S air-sea dynamic gravity meter system II.

Lee SJ, Chan YC, Komatitsch D, Huang BS, Tromp J (2009). Effects of realistic surface topography on seismic ground motion in the Yangminshan region of Taiwan based upon the spectral-element method and LiDAR DTM. Bulletin of the Seismological Society of America, 99(2A), 681-693.

Li J (2012). The recent Chinese terrestrial digital height datum model: gravimetric quasi-geoid CNGG2011. Acta Geodaetica et Cartographica Sinica, 41(5), 651-660.

Li X, Crowley JW, Holmes SA, Wang YM (2016). The contribution of the GRAV-D airborne gravity to geoid determination in the Great Lakes region. Geophysical Research Letters, 43(9), 4358-4365.

Li YS, Ning FS (2019). Research into GNSS levelling using network RTK in Taiwan. Survey Review, 51(364), 17-25.

Merwade V, Olivera F, Arabi M, Edleman S (2008). Uncertainty in flood inundation mapping: current issues and future directions. Journal of Hydrologic Engineering, 13(7), 608-620.

Milbert D (1995). Improvement of a high resolution geoid height model in the United States by GPS height on NAVD 88 benchmarks. Bulletin d'information-Bureau gravimétrique international(77), 13-36.

Miyahara B, Kodama T, Kuroishi Y (2014). Development of new hybrid geoid model for Japan,“GSIGEO2011”. Bulletin Geospatial Information Authority Japan, 62, 11-20.

Moritz H (1980). Advanced physical geodesy. Advances in Planetary Geology.

Pavlis NK, Holmes SA, Kenyon SC, Factor JK (2012). The development and evaluation of the Earth Gravitational Model 2008 (EGM2008). Journal of Geophysical research: solid earth, 117(B4).

Pavlis NK, Holmes SA, Kenyon SC, Factor JK (2013). Correction to The development and evaluation of the Earth Gravitational Model2008 (EGM2008). Journal of Geophysical Research: Solid Earth 118(5):2633. doi:10.1029/jgrb.50167Rapp RH, Balasubramania N (1992). A conceptual formulation of a world height system. Reports of the Department of Geodetic Science and Surveying(421).

Retscher G (2002). Accuracy performance of virtual reference station (VRS) networks. Journal of Global Positioning Systems, 1(1), 40-47.

Saleh J, Li X, Wang YM, Roman DR, Smith DA (2013). Error analysis of the NGS’surface gravity database. Journal of Geodesy, 87(3), 203-221.

Shih HC, Hwang C, Barriot JP, Mouyen M, Corréia P, Lequeux D, Sichoix L (2015). High-resolution gravity and geoid models in Tahiti obtained from new airborne and land gravity observations: data fusion by spectral combination. Earth, Planets and Space, 67(1), 124.

Shih TY, Peng MH, Wu SJ, Wu L (2005). The COA test flights of airborne LiDAR system in Taiwan. Journal of Photogrammetry and Remote Sensing, 10, 103-128.

Sjöberg LE(2000). Topographic effects by the Stokes–Helmert method of geoid and quasi-geoid determinations. Journal of Geodesy, 74(2), 255-268.

Tscherning CC, Rapp RH (1974). Closed covariance expressions for gravity anomalies, geoid undulations, and deflections of the vertical implied by anomaly degree variance models. Scientific Interim Report Ohio State Univ., Columbus. Dept. of Geodetic Science.

Webster TL, Forbes DL, Dickie S, Shreenan R (2004). Using topographic LiDAR to map flood risk from storm-surge events for Charlottetown, Prince Edward Island, Canada. Canadian Journal of Remote Sensing, 30(1), 64-76.

Wessel P, Smith WH (1998). New, improved version of Generic Mapping Tools released. Eos, Transactions American Geophysical Union, 79(47), 579-579.

Wong L, Gore R (1969). Accuracy of geoid heights from modified Stokes kernels. Geophysical Journal International, 18(1), 81-91.

Wu CR, Lu HF, Chao SY (2008). A numerical study on the formation of upwelling off northeast Taiwan. Journal of Geophysical Research: Oceans, 113(C8).

Yang M, Chen KH, Shiao SW (2003). A new height reference network in Taiwan. Survey Review, 37(290), 260-268.

Yang Y, Hwang C, Hsu HJ, Dongchen E, Wang H (2012). A subwaveform threshold retracker for ERS-1 altimetry: A case study in the Antarctic Ocean. Computers & geosciences, 41, 88-98.

Yeh TK, Chao BF, Chen CS, Chen CH, Lee ZY(2012). Performance improvement of network based RTK GPS positioning in Taiwan. Survey Review, 44(324), 3-8.

Zilkoski DB, Carlson E, Smith C (2008). Guidelines for Establishing GPS-derived Orthometric Heights: Standards 2 Cm and 5 Cm: Version 1.5: National Geodetic Survey.